Bayesian Inversion Using Global-Local Forward Models Applied to Fracture Propagation in Porous Media

Nima Noii, Amirreza Khodadadian, Thomas Wick

Leibniz Universität Hannover
Institute of Continuum Mechanics
An der Universität 1, 30823 Garbsen, Germany

Leibniz Universität Hannover
Institute of Applied Mathematics
Welfengarten 1, 30167 Hannover, Germany

Université Paris-Saclay, ENS Paris-Saclay
LMPS - Laboratoire de Mecanique Paris-Saclay
91190 Gif-sur-Yvette, France

Accepted for publication in
International Journal for Multiscale Computational Engineering (IJMCE)
in December 2021, published online March 2022
DOI: 10.1615/IntJMultCompEng.2022041735
URL: https://dl.begellhouse.com/journals/61fd1b191cf7e96f,forthcoming,41735.html
Under the Green Open Access Agreement

Bayesian Inversion Using Global-Local Forward Models Applied to Fracture Propagation in Porous Media

Nima Noii[a], Amirreza Khodadadian[b], Thomas Wick[b,c,1]

[a] Institute of Continuum Mechanics
Leibniz Universität Hannover, An der Universität 1, 30823 Garbsen, Germany

[b] Institute of Applied Mathematics
Leibniz Universität Hannover, Welfengarten 1, 30167 Hannover, Germany

[c] Université Paris-Saclay, ENS Paris-Saclay
LMT – Laboratoire de Mécanique et Technologie, 91190 Gif-sur-Yvette, France

Abstract

In this work, we are interested in parameter estimation in fractured media using Bayesian inversion. Therein, to reduce the computational costs of the forward model, a non-intrusive global-local approach is employed, rather than using fine-scale high-fidelity simulations. The crack propagates within the local region, and a linearized coarse model is employed in the global region. Here, a predictor-corrector mesh refinement approach is adopted, in which the local domain is dynamically adjusted to the current fracture state. Both subdomains change during the fluid injection time. Our algorithmic developments are substantiated with some numerical tests using phase-field descriptions of hydraulic fractures. The obtained results indicate that the global-local approach is an efficient technique for Bayesian inversion. It has the same accuracy as the full approach; however, the computational time is significantly lower.

Keywords: Bayesian inversion, global-local, multiscale, phase-field, hydraulic fractures, porous media

1. Introduction

Phase-field fracture is a very active research field with numerous applications. Overview articles and monographs include (Bourdin et al., 2008; Wu et al., 2019; Bourdin and Francfort, 2019; Wick, 2020; Francfort, 2021). In particular, fracture propagation due to internal pressures, i.e., hydraulic, is used worldwide for modeling processes in fractured porous media, extraction of oil and natural gases, waste storage, up to fluid-filled biomaterials. Such mathematical models are based on coupling fracture dynamics (modeling the displacement and crack propagation) and Darcy-type flow (modeling fluid pressure). For phase-field models in hydraulic fracture, we refer, for instance, to (Mikelić et al., 2013; Mikelić et al., 2015; Mikelić et al., 2015; Yoshioka and Bourdin, 2016; Lee et al., 2016, 2017; Wilson and Landis, 2016; Mikelić et al., 2019; Chukwudozie et al., 2019; Heider et al., 2018; Heider and Markert, 2017; Noii and Wick, 2019; Santillan et al., 2017). Recent overviews of phase-field fracture modeling in porous media and phase-field hydraulic fracturing were given in (Wheeler et al., 2020; Heider, 2021) and general overviews of hydraulic fracturing were performed in (Lecampion et al., 2018; Chen et al., 2021).

The mechanical and geomechanical parameters have an influential effect on the model simulations. Accurate information regarding these parameters yields a reliable model; however, inaccurate knowledge will lead to a wrong model response. Furthermore, due to the size of the porous medium (reservoir size), the parameters can fluctuate spatially. The domain of interest in fracking consists of different rock layers with a heterogeneous structure, which have different stiffness parameters (different Young's modulus and Poisson's ratio). Experimental estimation of these parameters is difficult and needs several efforts. Bayesian inversion is used to identify

[1]Corresponding author.

E-mail addresses: noii@ikm.uni-hannover.de (N. Noii); khodadadian@ifam.uni-hannover.de(A. Khodadadian); thomas.wick@ifam.uni-hannover.de (T. Wick)

the parameters based on a forward model (here PDE-based) and a backward probabilistic model (Smith, 2013). Markov chain Monte Carlo (MCMC) techniques are the most reliable statistical models to estimate the posterior distributions of the unknown parameters. We refer the interested readers to (Haario et al., 1999, 2006; Evensen, 2009; Green and Mira, 2001) for more details of about MCMC methods.

Recently, studies in parameter estimation (Khodadadian et al., 2020; Wu et al., 2021; Noii et al., 2021b,c) and stochastic phase-field fracture (Gerasimov et al., 2020), and numerical optimization (Neitzel et al., 2017, 2019; Khimin et al., 2021; Mohammadi and Wollner, 2020) have appeared in which phase-field fracture arises as forward model. A common challenge in these frameworks is that the forward problem must be solved numerous times again and again. In Bayesian inversion hundreds or thousand forward runs are necessary. In numerical optimization using adjoint methods, the adjoint problem is linear, but is running backward in time, resulting in a high computational cost. Consequently, the general natural idea is to use dimension reduction techniques such as model order reduction via, for instance, proper orthogonal decomposition based on the singular value decomposition (Abbaszadeh et al., 2021). A similar goal is achieved with the so-called non-intrusive global-local approach in which a fine-scale problem is solved in the fracture region and a linearized coarse problem in the remaining domain. Several papers have recently appeared from other groups (Geelen et al., 2020) and ourselves (Gerasimov et al., 2018; Noii et al., 2020; Aldakheel et al., 2021b,a).

In this work, we are going to utilize the lastly mentioned multiscale technique as dimension reduction. More specifically, rather than using high-fidelity finite element computations within each Bayesian iteration step, we employ the much less costly adaptive global-local multiscale approach as a forward model. Therein, the characteristic length of the local scale is of the same order as in the global part. In practice, the full (nonlinear) phase-field model is solved on the fine-scale, and a linearized model (without phase-field) is employed on the global scale. While the fracture propagates, the local and global subdomains are adjusted dynamically with the help of an adaptive predictor-corrector procedure (Noii et al., 2020). For hydraulic phase-field fracture forward models (not yet within Bayesian inversion) the multiscale procedure yielded wall clock run times of about 35 times faster in comparison to a full fine-scale computation while maintaining the same order of accuracy (Aldakheel et al., 2021b).

In (Noii et al., 2021c), we presented a Bayesian inversion setting to infer the effective mechanical and geomechanical parameters in hydraulic fracture. In (Aldakheel et al., 2021b), the authors developed a novel global-local multiscale method to model fracture during the fluid injection time. Here, we combine both procedures to model fracture in poroelastic media and estimate the parameters. To the best of our knowledge, using global-local multiscale as a cheap, but accurate, forward model within Bayesian inversion is accomplished the first time in the current paper. A flowchart of the overall framework is provided in Figure 1. We will study the effect of the multiscale technique on the parameter estimation by comparing the CPU (wall clock) time during different iterations when single-scale and multiscale frameworks are used. We expect that both approaches converge to a similar target density (since both have the same accuracy); however, the global-local method reduces the computational costs noticeably.

The outline of this paper is as follows: In Section 2, we introduce the mathematical model and describe how the phase-field fracture and pressure can be modeled in poroelastic media. In Section 3 we recapitulate the non-intrusive global-local approach. Next, in Section 4 our Bayesian inversion setting is explained and we discuss how a unified framework is obtained by combing the multiscale setting and the probabilistic model. In Section 5, a numerical test for hydraulic fracture is carried out to substaniate our main algorithm. Our work is summarized in Section 6.

2. Mathematical description for failure mechanics in poroelastic media

Let us consider $\mathcal{B} \in \mathbb{R}^{\delta}$ a solid in the Lagrangian configuration with dimension $\delta = 2$ in the spatial direction, time $t \in \mathcal{T} = [0, T]$ and $\partial\mathcal{B}$ its surface boundary. The given boundary-value problem (BVP) is a coupled multi-field system for the fluid-saturated porous media of the fracturing material. Fluid-saturated porous media can be formulated based on a coupled three-field system. At material points $\boldsymbol{x} \in \mathcal{B}$ and time $t \in \mathcal{T}$, the BVP solution indicates the displacement field $\boldsymbol{u}(\boldsymbol{x}, t)$ of the solid, the fluid pressure field $p(\boldsymbol{x}, t)$ and the phase-field fracture variable d can be represented by

$$\boldsymbol{u} : \begin{cases} \mathcal{B} \times \mathcal{T} \to \mathbb{R}^{\delta} \\ (\boldsymbol{x}, t) \mapsto \boldsymbol{u}(\boldsymbol{x}, t) \end{cases}, \quad p : \begin{cases} \mathcal{B} \times \mathcal{T} \to \mathbb{R} \\ (\boldsymbol{x}, t) \mapsto p(\boldsymbol{x}, t) \end{cases}, \quad d : \begin{cases} \mathcal{B} \times \mathcal{T} \to [0, 1] \\ (\boldsymbol{x}, t) \mapsto d(\boldsymbol{x}, t) \end{cases}. \tag{1}$$

Also $d(\boldsymbol{x}, t) = 0$ and $d(\boldsymbol{x}, t) = 1$ are referred to the unfractured as well as completely fractured part of the material, respectively. So, the coupled BVP is formulated through three specific primary fields to illustrate the hydro-poro-elasticity of fluid-saturated porous media by

$$\text{Global Primary Fields} : \mathfrak{U} := \{\boldsymbol{u}, p, d\}. \tag{2}$$

Additionally, for a given domain $\mathcal{B}$, we further assume a Neumann conditions as $\partial_N\mathcal{B} := \Gamma_N \cup \mathcal{C}$ with $\Gamma_N := \Gamma_N^{\boldsymbol{u}} \cup \Gamma_N^{p}$ which indicates the outer domain boundary for $(\boldsymbol{u}, p)$. Also, Dirichlet boundary conditions for both primary fields are defined as $\partial_D\mathcal{B} = \partial_D^{\boldsymbol{u}}\mathcal{B} \cup \partial_D^{p}\mathcal{B}$. We also denote the following spaces for stating the variational formulation:

$$\begin{aligned} &\texttt{deformation:} && \mathcal{W}_{\overline{\boldsymbol{u}}}^{\boldsymbol{u}} := \{\boldsymbol{u} \in \mathbf{H}^1(\mathcal{B}, \mathbb{R}^{\delta}) : \ \boldsymbol{u} = \overline{\boldsymbol{u}} \ \text{ on } \ \partial_D^{\boldsymbol{u}}\mathcal{B}\}, \\ &\texttt{fluid pressure:} && \mathcal{W}_{\overline{p}}^{p} := \{H^1(\mathcal{B}) \ : \ p = \bar{p} \ \text{ on } \ \partial_D^{p}\mathcal{B}\}, \\ &\texttt{phase-field:} && \mathcal{W}_{d_n}^{d} := \{d \in \mathrm{H}^1(\mathcal{B}, [0, 1]) : \ \ d \geq d_n\}. \end{aligned}$$

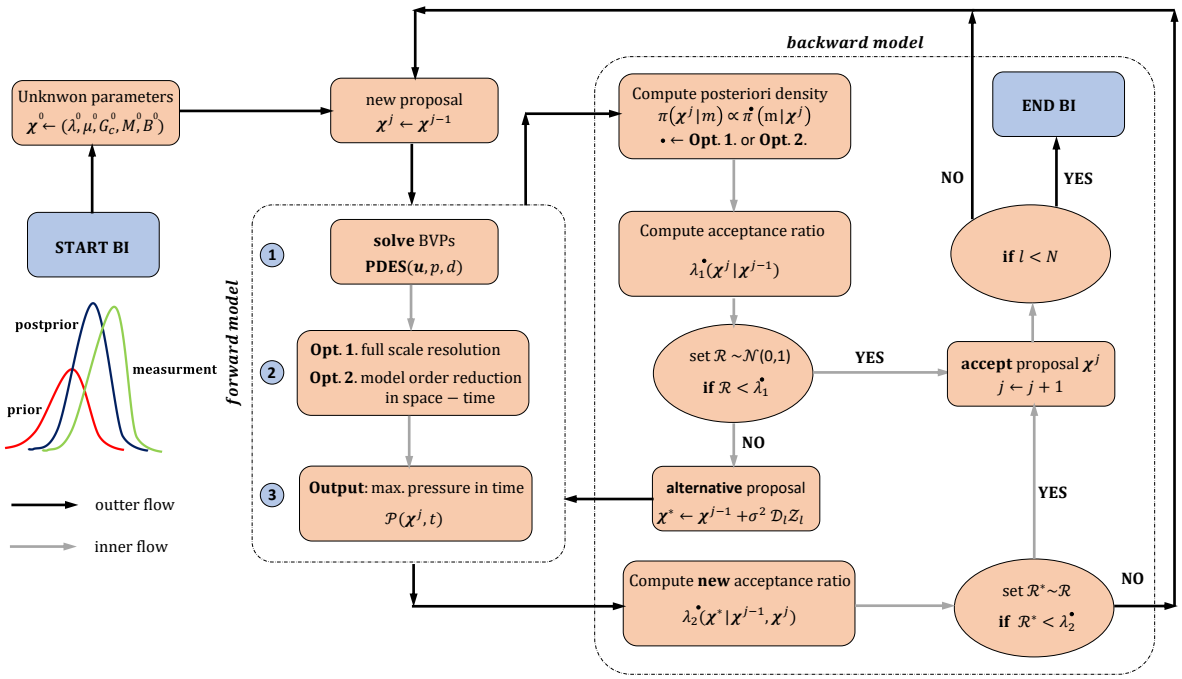

Figure 1: Bayesian Inversion (DRAM here, see Section 4) using global-local forward (see Section 3) adopted for the hydraulic fracture model (see Section 2).

2.1. Constitutive formulation in poroelastic media

To formulate constitutive energy density functions for poroelasticity, it suffices to define the total constitutive energy which additively decomposed into elastic contribution W_{elas}, fluid flow energy W_{fluid}, and fracture energy density W_{frac}. The total energy density function reads:

$$W(\mathfrak{C}) = W_{elas}(\boldsymbol{\varepsilon}, d) + W_{fluid}(\boldsymbol{\varepsilon}, \theta) + W_{frac}(d, \nabla d), \tag{3}$$

in terms of the following set

$$\text{Constitutive State Variables} : \mathfrak{C} := \{\boldsymbol{\varepsilon}, \theta, d, \nabla d\} \ , \tag{4}$$

to establish the multi-field evolution problem in terms of the primary fields functions. Here, the fluid volume ratio is represented by θ (fluid content) per unit volume of the given configuration $\mathcal{B}$. Also, the gradient of the displacement field defines the symmetric strain tensor of the geometrically linear theory as

$$\boldsymbol{\varepsilon} := \nabla_s \boldsymbol{u} = \text{sym}[\nabla \boldsymbol{u}] := \frac{1}{2}[\nabla \boldsymbol{u} + \nabla \boldsymbol{u}^T]. \tag{5}$$

To do so, first, we describe the elastic energy density W_{elas} is expressed in terms of the effective strain energy density ψ_{elas} by:

$$W_{elas}(\boldsymbol{\varepsilon}, d) = g(d)\ \psi(\boldsymbol{\varepsilon}) \quad \text{with} \quad \psi_{elas}(\boldsymbol{\varepsilon}) = \frac{\lambda}{2}(tr[\boldsymbol{\varepsilon}])^2 + \mu tr[\boldsymbol{\varepsilon}]^2. \tag{6}$$

Here, the standard monotonically decreasing quadrature degradation function is given as $g(d) := (1-d)^2 + \kappa$. Also, (λ, μ) are denoted as Lamé constants. Note that the small residual stiffness κ is introduced to prevent numerical instability problems. Next, following (Miehe and Mauthe, 2016; Mauthe and Miehe, 2017) the fluid density function takes the following quadrature form

$$W_{fluid}(\boldsymbol{\varepsilon}, \theta) = \frac{M}{2}\left[B^2 tr^2[\boldsymbol{\varepsilon}] - 2\,\theta\, tr[\boldsymbol{\varepsilon}] + \theta^2\right] = \frac{M}{2}\big(B\ tr[\boldsymbol{\varepsilon}] - \theta\big)^2, \tag{7}$$

based on the given fluid coefficient including which includes Biot's coefficient B and Biot's modulus M. Finally, within regularized fracture framework, a sharp-crack surface topology denoted by $\mathcal{C}$ to ensure the continuity of the crack field is further regularized by the smeared crack surface functional shown by $\mathcal{C}_l$ thus

$$\mathcal{C}_l(d) = \int_{\mathcal{B}} \gamma_l(d, \nabla d)\, dV \quad \text{with} \quad \gamma_l(d, \nabla d) := \frac{1}{2l} d^2 + \frac{l}{2} \nabla d \cdot \nabla d, \tag{8}$$

in terms of the regularized crack surface density function denoted by γ_l per unit volume of the solid and the regularization parameter l, so-called length scale, which governs the fracture diffusivity. So, the fracture contribution W_{frac} of the pseudo-energy density W, takes the following explicit form

$$W_{frac}(d, \nabla d) = G_c \gamma_l(d, \nabla d), \tag{9}$$

where $G_c > 0$ is so-called a Griffith's energy release rate. In the following, we describe the constitutive functions and corresponding strong forms for poroelastic media.

2.1.1 Elastic contribution

According to the classical Terzaghi theorem, the constitutive modeling corresponds to (6) results in the additive split of the stress tensor $\boldsymbol{\sigma}$ to effective mechanical contribution and fluid part as

$$\boldsymbol{\sigma}(\boldsymbol{\varepsilon}, p, d) := \frac{\partial W}{\partial \boldsymbol{\varepsilon}} = \boldsymbol{\sigma}_{eff} - Bp\boldsymbol{I} \quad \text{with} \quad \boldsymbol{\sigma}_{eff} = g(d)[\lambda tr\boldsymbol{\varepsilon}\boldsymbol{I} + 2\mu tr\boldsymbol{\varepsilon}]. \tag{10}$$

Thus, the balance of linear momentum for the multi-field system read

$$\boxed{\operatorname{Div}\boldsymbol{\sigma}(\boldsymbol{u}, p, d) + \overline{\boldsymbol{b}} = \boldsymbol{0}\,,} \tag{E}$$

such that dynamic motion is neglected (i.e., quasi-static response), and we denote $\overline{\boldsymbol{b}}$ as a prescribed body force.

2.1.2 Fluid contribution

The fluid volume flux vector is described through the negative direction of the gradient of the fluid pressure ∇p and permeability based on Darcy-type fluid's

$$\boldsymbol{\mathcal{F}} := -\boldsymbol{K}(\boldsymbol{\varepsilon}, d)\, \nabla p. \tag{11}$$

Here, the second-order permeability tensor (Miehe and Mauthe, 2016; Mauthe and Miehe, 2017) is additively decomposed into the permeability tensor into a Darcy-type flow for the unfractured porous medium $\boldsymbol{K}_{Darcy}$ and Poiseuille-type flow in a completely fractured material $\boldsymbol{K}_{frac}$ by:

$$\begin{aligned} \boldsymbol{K}(\boldsymbol{\varepsilon}, d) \quad &= \boldsymbol{K}_{Darcy} + d^{\zeta}\boldsymbol{K}_{frac}(\boldsymbol{\varepsilon}, d), \\ \boldsymbol{K}_{Darcy} \quad &= \tfrac{K_D}{\eta_F}\boldsymbol{I}, \\ \boldsymbol{K}_{frac}(\boldsymbol{\varepsilon}, d) \quad &= \big(\tfrac{\omega_d^2}{12\eta_F} - K_D\big)\ \big[\boldsymbol{I} - \boldsymbol{n}\otimes\boldsymbol{n}\big], \end{aligned} \tag{12}$$

Here, K_D is the isotopic intrinsic permeability of the pore space, η_F is the dynamic fluid viscosity and $\zeta \geq 1$ is a permeability transition exponent. Additionally, ω_d the so-called crack aperture (or the crack opening displacement) aligned with (Mauthe and Miehe, 2017; Xia et al., 2017) is defined as

$$\omega_d := [\![\boldsymbol{u}(\boldsymbol{x}).\boldsymbol{n}]\!] = (\boldsymbol{n}\cdot\boldsymbol{\varepsilon}\boldsymbol{n})h_e. \tag{13}$$

Also, $\boldsymbol{n} = \nabla d/|\nabla d|$ denotes the outward unit normal to the fracture surface, h_e is the characteristic discretization size, and $\boldsymbol{I}$ is an identity tensor. Following (Miehe and Mauthe, 2016), the conservation of the fluid mass, reflecting the fluid flow PDE within hydraulic fracturing setting reads

$$\dot{\theta}_F - \bar{r}_F + \operatorname{Div}[\boldsymbol{\mathcal{F}}] = 0\,. \tag{14}$$

This fluid-flow equation (14) is augmented with essential and natural boundary conditions. Thus, Dirichlet boundary conditions and Neumann boundary conditions for the pressure can be described by

$$p = \bar{p}(\boldsymbol{x}, t) \text{ on } \partial_D^p\mathcal{B} \quad \text{and} \quad \boldsymbol{\mathcal{F}}\cdot\boldsymbol{n} = \bar{f}(\boldsymbol{x}, t) \text{ on } \Gamma_N^p, \tag{15}$$

with an imposed fluid pressure $\bar{p}$ on the boundary surface, and fluid transport $\bar{f}$ on the Neumann boundary surface.

By employing the Coleman-Noll inequality condition in thermodynamics, the fluid pressure p is derived through

$$p(\boldsymbol{\varepsilon}, \theta) := \frac{\partial W}{\partial \theta} = \frac{\partial W_{fluid}}{\partial \theta} = \theta M - MBtr(\boldsymbol{\varepsilon}). \tag{16}$$

By condensing out θ in (14) based on p in (16), thus, the modified overall mass balance based on p reads

$$\boxed{\frac{\dot{p}}{M} + B\ \partial_t tr(\boldsymbol{\varepsilon}) - \bar{r}_F + \mathrm{Div}[\boldsymbol{\mathcal{F}}] = 0,} \tag{P}$$

which now depends on the fluid pressure p and not fluid volume fraction (porosity).

2.1.3 Fracture contribution

The crack driving state function in the regularizes sense conjugate to crack phase-field denoted as $D(\boldsymbol{\varepsilon}, d, \boldsymbol{x})$ for every point $\boldsymbol{x}$ in domain act as a driving force for the fracture evolution state reads

$$D(\boldsymbol{\varepsilon}, d, \boldsymbol{x}) := \frac{2l}{G_c}(1-\kappa)\psi_{elas}(\boldsymbol{\varepsilon}, \boldsymbol{x}). \tag{17}$$

align with (Mauthe and Miehe, 2017; Miehe et al., 2015). The maximum absolute value for the crack driving state function in time is defined by the time-dependent crack driving force $\mathcal{H}$ through

$$\mathcal{H} = \max_{s\in[0,t]} D(\boldsymbol{\varepsilon}(\boldsymbol{s}), d, \boldsymbol{x}) \geq 0. \tag{18}$$

So, the local evolution of the crack phase-field equation in the given domain $\mathcal{B}$ resulting from (8) augmented yields the third Euler-Lagrange differential system as

$$\boxed{(1-d)\mathcal{H} - [d - l^2\Delta d] = \eta\dot{d} \quad in\ \mathcal{B},} \tag{D}$$

augmented by the homogeneous Neumann boundary condition that is $\nabla d \cdot \boldsymbol{n} = 0$ on $\partial\mathcal{B}$.

2.1.4 Variational formulations for poroelastic media

The variational formulations with respect to the three PDEs (E-P-D) for the coupled poroelastic media of the fracturing material are derived by

$$\begin{aligned}
\mathcal{E}_{\boldsymbol{\varepsilon}}(\mathfrak{U}, \delta\boldsymbol{u}) &= \int_{\mathcal{B}} \Big[\boldsymbol{\sigma} : \delta\boldsymbol{\varepsilon} - \bar{\boldsymbol{b}} \cdot \delta\boldsymbol{u}\Big] dV - \int_{\Gamma_N} \bar{\boldsymbol{\tau}} \cdot \delta\boldsymbol{u}\ dA = 0, \\
\mathcal{E}_p(\mathfrak{U}, \delta p) &= \int_{\mathcal{B}} \Big[\Big(\frac{1}{M}(p - p_n) + B\big(tr(\boldsymbol{\varepsilon}) - tr(\boldsymbol{\varepsilon}_n)\big) - \Delta t\ \bar{r}_F\Big)\delta p + (\Delta t\ \boldsymbol{K}\ \nabla p) \cdot \nabla\delta p\Big] dV \\
&\quad + \int_{\partial_N\mathcal{B}} \Delta t \bar{f}\ \delta p\ dA = 0, \qquad \text{(SS)} \\
\mathcal{E}_d(\mathfrak{U}, \delta d) &= \Delta t \int_{\mathcal{B}} d\mathcal{H} \cdot \delta d V + \int_{\mathcal{B}} \Big[\Delta t(d - \mathcal{H}) \cdot \delta d + \eta(d - d_n) \cdot \delta d\Big]\ dV \\
&\quad + \int_{\mathcal{B}} \Big[l^2 \Delta t \nabla d \cdot \nabla(\delta d)\Big]\ dV = 0.
\end{aligned}$$

Remark 2.1. *For a similar system, a well-posedness analysis was conducted in (Mikelić et al., 2015). The major difference was the treatment of the crack irreversibility condition (here via the strain history function) and in (Mikelić et al., 2015) using penalization.*

2.1.5 Solution algorithms for the high-fidelity subproblems

In order to solve the high-fidelity hydraulic phase-field fracture system in (SS) within the global-local approach, we first solve the first two equations monolithically (simultaneously obtain $(\boldsymbol{u}, p)$). Then, a staggered approach is used to obtain the phase-field fracture d. To that end, we fix alternately $(\boldsymbol{u}, p)$ and estimate d and vice versa. The procedure is continued until convergence (using given $\texttt{TOL}_{\text{Stag}}$). For more details we refer the reader to our recent work in (Noii et al., 2021c) with the finite element discretization found Appendix A therein. Overall, we want to mention that the development and analysis of efficient and robust solvers for porous media problems are active and ongoing research fields. Particular studies include (Settari and Mourits, 1998; Settari and Walters, 2001; Dean et al., 2006; Kim et al., 2011; Mikelić and Wheeler, 2012; Dana et al., 2018; Almani et al., 2016; Dana and Wheeler, 2018a,b; Dana et al., 2021; Hong and Kraus, 2018; Both et al., 2017; Castelletto et al., 2015; Hong et al., 2020; Altmann et al., 2021; Lu and Wheeler, 2020), for fractured porous media (without phase-field) (Girault et al., 2016; Almani et al., 2021), and for phase-field fracture surrounded by porous media or pressure (Mikelić et al., 2015; Lee et al., 2017; Wheeler et al., 2020; Mikelić et al., 2015; Aldakheel et al., 2021b; Jammoul et al., 2021) (we mentioned here papers with a specific emphasis on solvers, for general papers on modeling, we refer the reader to the introduction). Moreover, basic phase-field solvers with an emphasis on $(\boldsymbol{u}, d)$ were proposed and analyzed in (Bourdin, 2007; Miehe et al., 2010; Mesgarnejad et al., 2015; Wick, 2017a,b; Kopanicakova and Krause, 2020; Brun et al., 2020; Gerasimov and Lorenzis, 2016; Jodlbauer et al., 2020a; Wambacq et al., 2021; Kristensen and MartÃnez-Paneda, 2020; Lampron et al., 2021; Jodlbauer et al., 2020b; Jodlbauer, 2021). These developments remain important since within model order reduction problems, such as global-local techniques, the high-fidelity subproblems must still be solved in an accurate, robust, and efficient fashion.

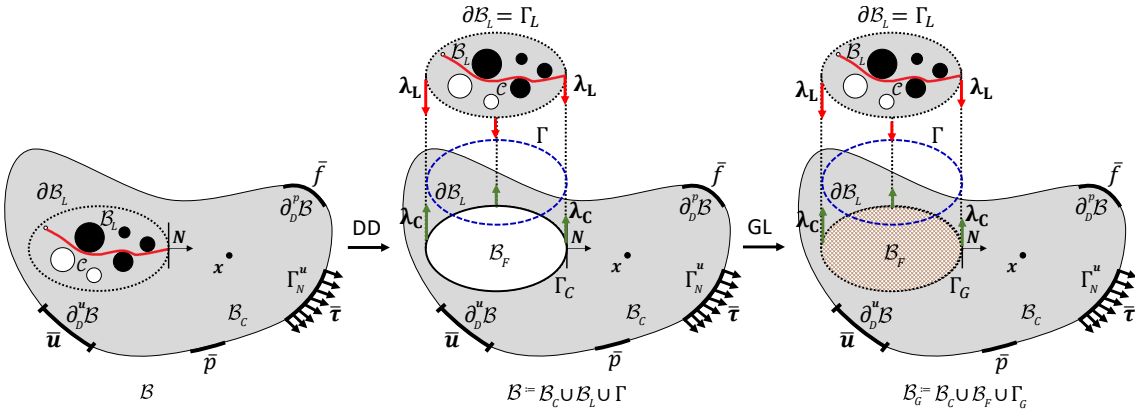

Figure 2: Description of the global-local setting. Left: Configuration and loading setup of the single-scale BVP. Right: global-local configuration, by means of the fictitious domain $\mathcal{B}_F$ through filling the gap between $\mathcal{B}_C$ and $\mathcal{B}_L$ with a same constitutive modeling and discretization of $\mathcal{B}_C$ such that its unification is a so-called global domain $\mathcal{B}_G := \mathcal{B}_C \cup \Gamma_G \cup \mathcal{B}_F$.

3. Global-local phase-field fracture in poroelastic media

The previously introduced system of equations for single-scale analysis in (SS) for the coupled problem of poroelasticity and fracture is solved is further extended toward the global-local (GL) method in this section. Following (Gerasimov et al., 2018; Noii et al., 2020; Aldakheel et al., 2021b) the GL formulation is rooted in domain decomposition approaches by distinguishing the original domain into coarse and fine discretizations, see Figure 2.

Since in the GL formulation there are two different *disjoint domains in space*, denoted as a global domain $\mathcal{B}_G$ (characterized with coarse mesh) with its boundary Γ_G, and also a local domain $\mathcal{B}_L$ (characterized with fine mesh) with its boundary Γ_L, the coupling conditions are further required. Notably, the fictitious domain $\mathcal{B}_F$ is defined as a prolongation of a complimentary domain towards $\mathcal{B}$. Hence, it recovers the space of $\mathcal{B}$ that is obtained by removing the local domain from its continuum scale, see Fig. 2. To do so, we have introduced an additional auxiliary interface denoted as Γ between two disjoint domains in poroelastic media (see (Aldakheel et al., 2021b)), and thus corresponding unknown fields, see Figure 2. These additional fields are the interface deformation $\boldsymbol{u}_\Gamma(\boldsymbol{x},t)$ and pressure $p_\Gamma(\boldsymbol{x},t)$ on auxiliary interface and their corresponding traction forces $\{\boldsymbol{\lambda}^{\boldsymbol{u}}_L, \boldsymbol{\lambda}^{\boldsymbol{u}}_C\}$ and $\{\lambda^p_L, \lambda^p_C\}$ that are introduced as Lagrange multipliers. This results in a set of coupling equations at the interface by

$$\left\{\begin{array}{lll} \boldsymbol{u}_L(\boldsymbol{x},t) = \boldsymbol{u}_\Gamma(\boldsymbol{x},t) & \text{at } \boldsymbol{x}\in\Gamma_L, & \\ \boldsymbol{u}_G(\boldsymbol{x},t) = \boldsymbol{u}_\Gamma(\boldsymbol{x},t) & \text{at } \boldsymbol{x}\in\Gamma_G, & \text{and} \\ \boldsymbol{\lambda}^{\boldsymbol{u}}_L(\boldsymbol{x},t) + \boldsymbol{\lambda}^{\boldsymbol{u}}_C(\boldsymbol{x},t) = \boldsymbol{0} & \text{at } \boldsymbol{x}\in\Gamma, & \end{array}\right. \quad \left\{\begin{array}{ll} p_L(\boldsymbol{x},t) = p_\Gamma(\boldsymbol{x},t) & \text{at } \boldsymbol{x}\in\Gamma_L, \\ p_G(\boldsymbol{x},t) = p_\Gamma(\boldsymbol{x},t) & \text{at } \boldsymbol{x}\in\Gamma_G, \\ \lambda^p_L(\boldsymbol{x},t) + \lambda^p_C(\boldsymbol{x},t) = 0 & \text{at } \boldsymbol{x}\in\Gamma. \end{array}\right. \tag{19}$$

Now, the multi-physics problem for the global-local approach is described through eleven primary fields to characterize the hydro-poro-elasticity of fluid-saturated porous media at finite strains by

$$\text{Extended Primary Fields}: \mathfrak{P} := \{\boldsymbol{u}_G, \boldsymbol{u}_L, p_G, p_L, d_L, \boldsymbol{\lambda}^{\boldsymbol{u}}_C, \boldsymbol{\lambda}^{\boldsymbol{u}}_L, \lambda^p_C, \lambda^p_L, \boldsymbol{u}_\Gamma, p_\Gamma\}\ . \tag{20}$$

Herein, a global constitutive model behaves as a poroelastic response, abbreviated as E(elastic)-P(pressure), which is augmented with a *single local domain* and behaves as a poroelastic material with fracture response, abbreviated as E(elastic)-P(pressure)-D(damage).

3.1. Local problem (L-EPD)

Next, we illustrate that the local weak formulations take the following variational form

$$\begin{aligned}
\widehat{\mathcal{E}}_{\boldsymbol{u}_L}(\mathfrak{P},\delta\boldsymbol{u}_L) &:= \int_{\mathcal{B}_L} \boldsymbol{\sigma}(\nabla\boldsymbol{u}_L, p_L, d_L) : \nabla\delta\boldsymbol{u}_L \mathrm{d}V - \int_{\Gamma_L} \boldsymbol{\lambda}^{\boldsymbol{u}}_L \cdot \delta\boldsymbol{u}_L \,\mathrm{d}A = 0\ , \\
\widehat{\mathcal{E}}_{p_L}(\mathfrak{P},\delta p_L) &:= \int_{\mathcal{B}_L} \Big[\frac{1}{M}(p_L - p_{L,n}) + B\Big(\boldsymbol{\varepsilon}(\boldsymbol{u}_L) - \boldsymbol{\varepsilon}_n(\boldsymbol{u}_L)\Big)\Big]\delta p_L \ \mathrm{d}V \\
&\quad + \int_{\mathcal{B}_L} \Big[\Big(\Delta t\ \boldsymbol{K}(\boldsymbol{\varepsilon}_L, d_L)\ \nabla p_L\Big)\cdot\nabla\delta p_L\Big]\mathrm{d}V - \int_{\Gamma_L} \lambda^p_L\ \delta p_L \,\mathrm{d}A = 0, \\
\widehat{\mathcal{E}}_{d_L}(\mathfrak{P},\delta d_L) &:= \Delta t \int_{\mathcal{B}_L} \Big[d_L\mathcal{H}\cdot\delta d V\Big] + \int_{\mathcal{B}} \Big[\Delta t(d_L - \mathcal{H})\cdot\delta d_L + \eta(d_L - d_{L,n})\cdot\delta d_L\Big]\ dV \\
&\quad + \int_{\mathcal{B}_L} \Big[l^2\Delta t\nabla d_L\cdot\nabla(\delta d_L)\Big]\ dV = 0\ ,
\end{aligned} \tag{L}$$

where $\delta\boldsymbol{u}_L \in \boldsymbol{H}^1(\mathcal{B}_L)$, $\delta p_L \in H^1(\mathcal{B}_L)$ and $\delta d_L \in H^1(\mathcal{B}_L)$ are the local test functions with respect to the local deformation $\boldsymbol{u}_L$, local fluid pressure p_L and local crack phase-field d_L, respectively.

3.1.1 Robin-type boundary conditions at the local level

The local BVP given in (L) is still incomplete. Thus, we augment (L) with coupling terms, so results in the following boundary conditions for local deformation field by

$$\int_\Gamma \boldsymbol{\lambda}_L^{\boldsymbol{u},k} \cdot \delta \boldsymbol{u}_\Gamma \,\mathrm{d}A + \mathcal{A}_L^{\boldsymbol{u}} \int_\Gamma \boldsymbol{u}_\Gamma^{k,\frac{1}{2}} \cdot \delta \boldsymbol{\lambda}_C^{\boldsymbol{u}} \,\mathrm{d}A = \boldsymbol{\Lambda}_L^{\boldsymbol{u},k-1}, \tag{C.L.E$_1$}$$

$$\int_\Gamma (\boldsymbol{u}_\Gamma^{k,\frac{1}{2}} - \boldsymbol{u}_L^k) \cdot \delta \boldsymbol{\lambda}_L^{\boldsymbol{u}} \,\mathrm{d}A = 0, \tag{C.L.E$_2$}$$

with

$$\boldsymbol{\Lambda}_L^{\boldsymbol{u},k-1} := \boldsymbol{\Lambda}_L(\boldsymbol{\lambda}_C^{\boldsymbol{u},k-1}, \boldsymbol{u}_G^{k-1}; \mathcal{A}_L^{\boldsymbol{u}}) = \mathcal{A}_L^{\boldsymbol{u}} \int_\Gamma \boldsymbol{u}_G^{k-1} \cdot \delta \boldsymbol{\lambda}_C^{\boldsymbol{u}} \,\mathrm{d}A - \int_\Gamma \boldsymbol{\lambda}_C^{\boldsymbol{u},k-1} \cdot \delta \boldsymbol{u}_\Gamma \,\mathrm{d}A \,. \tag{21}$$

Analogously to the coupling terms for the global fluid pressure in (C.G.P), we introduce the local coupling system of equations for the pressure field at the interface through

$$\int_\Gamma \lambda_L^{p,k} \,\delta p_\Gamma \,\mathrm{d}A + \mathcal{A}_L^{p} \int_\Gamma p_\Gamma^{k,\frac{1}{2}} \,\delta \lambda_C^{p} \,\mathrm{d}A = \Lambda_L^{p,k-1}, \tag{C.L.P$_1$}$$

$$\int_\Gamma (p_\Gamma^{k,\frac{1}{2}} - p_L^k) \delta \lambda_L^p \,\mathrm{d}A = 0, \tag{C.L.P$_2$}$$

with

$$\Lambda_L^{p,k-1} := \Lambda_L(\lambda_C^{p,k-1}, p_G^{k-1}; \mathcal{A}_L^{p}) = \mathcal{A}_L^{p} \int_\Gamma p_G^{k-1} \delta \lambda_C^{p} \,\mathrm{d}A - \int_\Gamma \lambda_C^{p,k-1} \delta p_\Gamma \,\mathrm{d}A. \tag{22}$$

In summary, an *enhanced local* BVP has the following abstract form,

$$\texttt{L-EPD:} \quad (\boldsymbol{u}_L^k, p_L^k, \boldsymbol{\lambda}_L^{\boldsymbol{u},k}, \lambda_L^{p,k}, \boldsymbol{u}_\Gamma^{k,\frac{1}{2}}, p_\Gamma^{k,\frac{1}{2}}) = \texttt{L}(\boldsymbol{\Lambda}_L^{\boldsymbol{u},k-1}, \Lambda_L^{p,k-1}, \mathcal{A}_L^{\boldsymbol{u}}, \mathcal{A}_L^{p}) \,, \tag{23}$$

such that, at $k = 0$ the global-local formulation is initialized with the previous converged solution at $n-1$, so $\mathfrak{P}_n^0 = \mathfrak{P}_{n-1}$ (for simplicity of notation, we dropped n in the formulation). Here, ($\mathcal{A}_L^{\boldsymbol{u}}$, $\mathcal{A}_L^{p}$, $\boldsymbol{\Lambda}_L^{\boldsymbol{u},k}$, $\Lambda_L^{p,k}$) stand for local Robin-type parameters (for the derivation of Robin-type parameters see (Noii et al., 2020)).

3.2. Global problem (G-EP)

Based on the above-introduced decompositions and the weak formulations outlined in (SS), this section describes the *global weak forms* of the PDEs for the coupled problem and its *coupling Robin-type boundary conditions*. Following (Aldakheel et al., 2021b), the global weak formula-

tions of the deformation and pressure field take the form

$$
\begin{aligned}
\widehat{\mathcal{E}}_{\boldsymbol{u}_G}(\mathfrak{P}, \delta\boldsymbol{u}_G) &:= \int_{\mathcal{B}_G} \boldsymbol{\sigma}(\nabla\boldsymbol{u}_G, p_G, 0) : \nabla\delta\boldsymbol{u}_G \mathrm{d}V - \int_{\mathcal{B}_F} \boldsymbol{\sigma}(\nabla\boldsymbol{u}_G, p_G, 0) : \nabla\delta\boldsymbol{u}_G \mathrm{d}V \\
&\quad - \int_{\Gamma_G} \boldsymbol{\lambda}_C^{\boldsymbol{u}} \cdot \delta\boldsymbol{u}_G \, \mathrm{d}A - \int_{\Gamma_{N,G}} \bar{\boldsymbol{\tau}} \cdot \delta\boldsymbol{u}_G \, \mathrm{d}A = 0 \ , \\
\widehat{\mathcal{E}}_{p_G}(\mathfrak{P}, \delta p_G) &:= \int_{\mathcal{B}_G} \Big[\frac{1}{M}(p_G - p_{G,n}) + B\Big(tr(\boldsymbol{\varepsilon})(\boldsymbol{u}_G) - tr(\boldsymbol{\varepsilon}_n)(\boldsymbol{u}_G)\Big)\Big]\delta p_G \ \mathrm{d}V \\
&\quad + \int_{\mathcal{B}_G} \Big[(\Delta t \ \boldsymbol{K}(\boldsymbol{\varepsilon}_G, 0) \ \nabla p_G) \cdot \nabla\delta p_G\Big]\mathrm{d}V \\
&\quad - \int_{\mathcal{B}_F} \Big[\frac{1}{M}(p_G - p_{G,n}) + + B\Big(tr(\boldsymbol{\varepsilon})(\boldsymbol{u}_G) - tr(\boldsymbol{\varepsilon}_n)(\boldsymbol{u}_G)\Big) + \Delta t \ \bar{r}_F\Big]\delta p_G \ \mathrm{d}V \\
&\quad - \int_{\mathcal{B}_F} \Big[(\Delta t \ \boldsymbol{K}(\boldsymbol{\varepsilon}_G, 0) \ \nabla p_G) \cdot \nabla\delta p_G\Big]\mathrm{d}V \\
&\quad - \int_{\Gamma_G} \lambda_C^p \ \delta p_G \, \mathrm{d}A + \int_{\Gamma_{N,G}} \bar{f} \ \delta p_G \ dA = 0 \ ,
\end{aligned}
\tag{G}
$$

where $\delta\boldsymbol{u}_G \in \{\boldsymbol{H}^1(\mathcal{B}_G)^\delta : \delta\boldsymbol{u}_G = \boldsymbol{0} \text{ on } \partial_D\mathcal{B}\}$ and $\delta p_G \in \{H^1(\mathcal{B}_G) : \delta p_G = 0 \text{ on } \partial_D\mathcal{B}\}$ are the global test functions. Note that the pressure injection process of hydraulic fracturing $\bar{r}_F$ *exists only* in the fictitious domain $\mathcal{B}_F$.

3.2.1 Robin-type boundary conditions at the global level

We continue to formulate the Robin-type boundary condition at the global level follows:

$$
\int_\Gamma \boldsymbol{\lambda}_C^{\boldsymbol{u},k} \cdot \delta\boldsymbol{u}_\Gamma \, \mathrm{d}A + \mathbb{A}_G^{\boldsymbol{u}} \int_\Gamma \boldsymbol{u}_\Gamma^k \cdot \delta\boldsymbol{\lambda}_L^{\boldsymbol{u}} \, \mathrm{d}A = \boldsymbol{\Lambda}_G^{\boldsymbol{u},k}, \tag{C.G.E$_1$}
$$

$$
\int_\Gamma (\boldsymbol{u}_\Gamma^{k,\frac{1}{2}} - \boldsymbol{u}_G^k) \cdot \delta\boldsymbol{\lambda}_C^{\boldsymbol{u}} \, \mathrm{d}A = 0, \tag{C.G.E$_2$}
$$

with

$$
\boldsymbol{\Lambda}_G^{\boldsymbol{u},k} := \boldsymbol{\Lambda}_G(\boldsymbol{\lambda}_L^{\boldsymbol{u},k}, \boldsymbol{u}_L^k; \mathbb{A}_G^{\boldsymbol{u}}) = \mathbb{A}_G^{\boldsymbol{u}} \int_\Gamma \boldsymbol{u}_L^k \cdot \delta\boldsymbol{\lambda}_L^{\boldsymbol{u}} \, \mathrm{d}A - \int_\Gamma \boldsymbol{\lambda}_L^{\boldsymbol{u},k} \cdot \delta\boldsymbol{u}_\Gamma \, \mathrm{d}A \ . \tag{24}
$$

Following the procedure outlined in (Aldakheel et al., 2021b), the Robin-type boundary condition at the global level for the pressure field yields

$$
\int_\Gamma \lambda_C^{p,k} \ \delta p_\Gamma \, \mathrm{d}A + \mathbb{A}_G^p \int_\Gamma p_\Gamma^k \ \delta\lambda_L^p \, \mathrm{d}A = \Lambda_G^{p,k}, \tag{C.G.P$_1$}
$$

$$
\int_\Gamma (p_\Gamma^{k,\frac{1}{2}} - p_G^k)\delta\lambda_C^p \, \mathrm{d}A = 0, \tag{C.G.P$_2$}
$$

with

$$
\Lambda_G^{p,k} := \Lambda_L(\lambda_L^{p,k}, p_L^k; \mathbb{A}_G^p) = \mathbb{A}_G^p \int_\Gamma p_L^k \delta\lambda_L^p \, \mathrm{d}A - \int_\Gamma \lambda_L^{p,k} \delta p_\Gamma \, \mathrm{d}A. \tag{25}
$$

In summary, an *enhanced global* BVP has the following abstract form,

$$
\texttt{G-EP:} \quad (\boldsymbol{u}_G^k, p_G^k, \boldsymbol{\lambda}_C^{\boldsymbol{u},k}, \lambda_C^{p,k}, \boldsymbol{u}_\Gamma^k, p_\Gamma^k) = \texttt{G}(\boldsymbol{u}_\Gamma^{k,\frac{1}{2}}, p_\Gamma^{k,\frac{1}{2}}, \boldsymbol{\Lambda}_G^{\boldsymbol{u},k}, \Lambda_G^{p,k}, \mathbb{A}_G^{\boldsymbol{u}}, \mathbb{A}_G^p) \ , \tag{26}
$$

such that, at $k = 0$ the global-local formulation is initialized with the previous converged solution at $n-1$. Here, ($\mathbb{A}_G^{\boldsymbol{u}}$, $\mathbb{A}_G^{p}$, $\mathbf{\Lambda}_G^{\boldsymbol{u},k}$, $\Lambda_G^{p,k}$) stand for global Robin-type parameters.

Thus, we are now able to formulate the global-local formulation through the coupling between a global domain with a single local domain in the following abstract form:

$$\boxed{\mathfrak{P}_n = \mathtt{GL}(\mathfrak{P}_{n-1}) := \mathtt{L}(\mathfrak{P}_{n-1}^k) + \mathtt{G}(\mathfrak{P}_{n-1}^k)\ .} \tag{GL}$$

3.2.2. Predictor-corrector mesh adaptivity in GL. Following (Noii et al., 2020; Aldakheel et al., 2021b), to further reduce the computational cost, an adaptive global-local approach is employed. For doing so, a predictor-corrector mesh adaptivity is preformed at t_n through *dynamically allocation* of a local domains. More precisely, by predictor-corrector mesh adaptivity, we mean: (i) to determine for which local edges in the local domain, the phase-field value reached to its threshold; (ii) to identify which global elements need to be refined (those global elements which share the same edges with determined local edges); (iii) to create the new fictitious and local domains, (iv) to determine new local and global interfaces; (v) to interpolate the old global solution at t_n towards the local domain for initialization. For a detail discussion, we refer the interested reader to (Noii et al., 2021a, 2020).

4. Bayesian inversion

Bayesian inversion has been used in different applied and engineering problems to identify specific material parameters that either cannot be measured with usual techniques, or for which significant experimental efforts are needed to provide a reasonable estimation (Green and Worden, 2015). In this section, we review the Bayesian inversion setting used to identify material parameters in mechanical models. As the first step, we present a statistical model

$$\mathcal{M} = \mathcal{P}(\Theta) + \varepsilon, \tag{27}$$

where $\mathcal{M}$ indicate the reference observation (arising from a measured data of a given synthetic value), $\mathcal{P}$, is the model response (estimated by an observation from the model equation, here hydraulic fracture), and ε points out the measurement error. Since $\mathcal{P}$ in (27) is a model response which results in our computation, such that in our presented model can be approximated through

$$\texttt{signle-scale simultation:}\quad \mathcal{P} \approx \mathcal{P}^{\mathrm{SS}} \quad \text{or} \quad \texttt{global-local simulation:}\quad \mathcal{P} \approx \mathcal{P}^{\mathrm{GL}},$$

corresponds to equations (SS) and (GL), respectively. Thus, (27) becomes as

$$\mathcal{M} = \mathcal{P}^{\bullet}(\Theta) + \varepsilon, \quad \text{with} \quad \bullet \in \{\mathrm{SS},\mathrm{GL}\}. \tag{28}$$

In this probabilistic model, the main aim is to determine the material parameter χ (in our case $\chi \in (\lambda,\, \mu,\, G_c,\, M,\, B) \subset \Theta$), which is a realization of the set of parameters Θ. The error of the measurement is normally distributed, i.e., $\mathcal{N}(0, \sigma^2\mathbf{I})$ where σ^2 denotes a fidelity parameter and indicates the level of measurement error. We assume to have a Lebesgue density π and the conditional density is given by

$$\pi(\chi|m) = \frac{\pi(\chi, m)}{\pi(m)}, \tag{29}$$

in the sense that

$$\pi(m) = \int_{\mathbb{R}^W} \pi(m,\chi)\ \pi_0(\chi)\,\mathrm{d}\,\chi, \tag{30}$$

where $\pi_0(\chi)$ is the *prior* probability density, and W is the space of the unknown parameters. If we consider a measured value m using the Bayes theorem concludes the *posteriori* density as

$$\pi(\chi|\, m) = \frac{\pi(m|\, \chi)\pi_0(\chi)}{\pi(m)} = \frac{\pi(m|\, \chi)\pi_0(\chi)}{\displaystyle\int_{\mathbb{R}^W} \pi(m, \chi)\ \pi_0(\chi)\, \mathrm{d}\, \chi}. \tag{31}$$

The denominator is a normalization constant and its computation can be neglected. Thus, the posterior density is proportional to the likelihood function and the prior distribution, i.e.,

$$\pi(\chi|\, m) \propto \pi(m|\, \chi)\pi_0(\chi).$$

We consider that the errors have the independent and identically distribution (i.e., $\varepsilon_i \sim N(0, \sigma^2)$). Considering the multiscale setting (the solution obtained by SS or GL), the likelihood function is computed as

$$\pi^{\bullet}(m|\, \chi) := \frac{1}{(2\pi\sigma^2)^{n/2}} \exp(-\zeta^{\bullet}(\chi)/2\sigma^2) \quad \text{with} \quad \bullet \in \{\text{SS,GL}\}, \tag{32}$$

where

$$\zeta(\chi)^{\bullet} = \sum_{i=1}^{n} |\, m_i - \mathcal{I}_i^{\bullet}(\chi)\,|^2 \quad \text{for} \quad i = 1, \ldots, n \quad \text{with} \quad \bullet \in \{\text{SS,GL}\}. \tag{33}$$

Here, n denotes the incremental steps (time steps) in our rate-dependent problem. We note that (33) is a crucial parameter that indicates the difference between the reference value (such as a measured value) and the model response (here a PDE-based model) with respect to the (proposed) candidate χ. During different time-steps ($i = 1, \ldots, n$), more difference between the reference observation m_i and the realizations with respect to the proposal $\mathcal{I}_i(\chi)$ will reduce the probability of the happening (likelihood function). An efficient way to provide informative information about the parameters is using the MCMC (Markov Chain Monte Carlo) techniques. Here, according to a proposal distribution, several parameters are proposed, and based on the likelihood function, the algorithm determines that they should be accepted (kept in the MCMC chain) or rejected (the chain is followed with the previously accepted candidate). The most common and trivial MCMC method is Metropolis-Hastings (MH) algorithm, which is given in Algorithm 1.

Although the MH algorithm can be implemented easily, it is computationally not effective specifically when a multi-dimensional set of parameters must be inferred simultaneously. In fact, in this algorithm, the proposal distribution (ϕ) is related to the Cholesky decomposition of the given (fixed) proposal density, and will not be changed during the sampling process . If the initial covariance matrix is not chosen accurately, several candidates will be rejected. As a result, the acceptance rate reduces significantly, and the method efficiency will be reduced. To overcome this problem, based on the obtained information from the proposal density can be updated in each iteration or at desired iterations (e.g., every 100 iterations). This global adaptation will enable us to enhance the acceptance rate, specifically obeying useless candidates' rejection. To improve the method's effectiveness a local adaptation can be combined. If a proposed value is rejected, we can change slightly the chain direction and provide an alternative for the rejected candidate. Giving another chance to this proposal can be performed once or can be repeated more. We provide a summary of the delayed rejection adaptive Metropolis-Hastings (DRAM) model in Algorithm 2.

In DRAM algorithm, $\mathcal{Z}_j \sim$ Uniform $(0, \boldsymbol{I}_N)$ where $\boldsymbol{I}_N$ is the N-dimensional identity matrix. In order to use a narrower proposal distribution (compared to the initial proposal) we use $\sigma < 1$.

Algorithm 1 The MH algorithm.

Initialization ($j = 0$): start with the $\chi^0 \sim \pi^\bullet(\chi^0|\, m)$ with $\bullet \in \{\text{SS,GL}\}$.

For $j < N$

1. $j = j + 1$.
2. Produce a new proposal according to the proposal density $\chi^* \sim \phi(\chi^j|\, \chi^{j-1})$.
   2.1. Solve the system of equations (SS) or (GL) and obtain $(\boldsymbol{u}, p, d)$ according to the realization $\chi^* \in \{\lambda, \mu, G_c, M, B\}$.
3. Compute the acceptance/rejection ratio

$$\lambda^\bullet(\chi^*|\, \chi^{j-1}) = \min\left(1, \frac{\pi^\bullet(\chi^*|\, m)\phi(\chi^{j-1}|\, \chi^*)}{\pi^\bullet(\chi^{j-1}|\, m)\phi(\chi^*|\, \chi^{j-1}))}\right)$$

.

5. Produce a uniform random variable between 0 and 1 ($\mathcal{R}$).
6. **if** $\mathcal{R} < \lambda$ **then**

   accept the proposal χ^* and follow the chain with $\chi^j = \chi^*$

   else

   reject the proposal χ^* and follow the chain with $\chi^j = \chi^{j-1}$

   end if

We can calculate the covariance function by

$$\mathcal{COV}_j = \text{Cov}(\chi^0, \chi^1, \ldots, \chi^j) := \frac{1}{j}\left(\sum_{i=0}^{j} \chi^i \left(\chi^i\right)^T - (j+1)\, \hat{\chi}^j \left(\hat{\chi}^j\right)^T\right), \tag{34}$$

where $\hat{\chi}^j = \dfrac{1}{j+1}\displaystyle\sum_{i=0}^{j} \chi^i$. We refer the interested reader to (Haario et al., 2006) for more details. We note that other optimization approaches can be used to determine intrinsic material properties from experimental observation, see e.g., (Noii and Aghayan, 2019) and references therein.

So, the unknown material parameters $\chi \in (\lambda,\, \mu,\, G_c,\, M,\, B) \subset \Theta$ for poroelastic fracturing media are estimated through the probabilistic Bayesian inversion (BI) model using either single-scale (SS) or global-local (GL) forward model through the following abstract form:

$$\boxed{\texttt{BI-SS}: \quad \chi \leftarrow \texttt{BI(SS}(\mathfrak{U})) \quad \text{and} \quad \texttt{BI-GL}: \quad \chi \leftarrow \texttt{BI(GL}(\mathfrak{P}))}$$

5. Numerical simulations

In this section, we investigate a numerical test with the main goal that Bayesian inversion yields accurate parameter identifications at a cheap cost of the governing global-local phase-field

Algorithm 2 The DRAM algorithm.

Initialization ($j = 0$): Generate the initial parameter $\chi^0 \sim \pi^\bullet(\chi^0|\, m)$ with $\bullet \in \{\text{SS,GL}\}$.

For $j < N$

1. $j = j + 1$.
2. Use the Cholesky decomposition to produce the new proposal as $\chi^* = \chi^{j-1} + \mathcal{D}_j \mathcal{Z}_j$.
   2.1. Solve the system of equations (SS) or (GL) and obtain $(\boldsymbol{u}, p, d)$ according to the realization $\chi^* \in \{\lambda, \mu, G_c, M, B\}$.
3. Compute the acceptance/rejection ratio

$$\lambda_1^\bullet(\chi^*|\, \chi^{j-1}) = \min\left(1, \frac{\pi^\bullet(\chi^*|\, m)\ \phi(\chi^{j-1}|\ \chi^*)}{\pi^\bullet(\chi^{j-1}|\, m)\ \phi(\chi^*|\, \chi^{j-1}))}\right).$$

4. Produce $\mathcal{R}$ a uniform random variable between 0 and 1.
5. **if** $\mathcal{R} < \lambda_1$ **then**

   accept the proposal χ^* and follow the chain with $\chi^j = \chi^*$

   else

   1. Compute the alternative proposal

$$\chi^{**} = \chi^{j-1} + \sigma^2 \mathcal{D}_j \mathcal{Z}_j.$$

   2. Compute the acceptance/rejection ratio

$$\lambda_2^\bullet(\chi^{**}|\, \chi^{j-1}, \chi^*) = \min\left(1, \frac{\pi^\bullet(\chi^{**}|\, m)\ \phi(\chi^*|\ \chi^{**})\,(1 - \lambda_1^\bullet(\chi^*|\chi^{**}))}{\pi^\bullet(\chi^{j-1}|\, m)\ \phi(\chi^*|\ \chi^{j-1})\,(1 - \lambda_1^\bullet(\chi^*|\chi^{j-1}))}\right).$$

   3. **if** $\mathcal{R} < \lambda_2$ **then**

      accept the proposal χ^* and follow the chain with $\chi^j = \chi^*$

      else

      reject the proposal χ^* and follow the chain with $\chi^j = \chi^{j-1}$

      end if

   end if

6. Calculate the updated $\mathcal{COV}_j = \text{Cov}(\chi^0, \chi^1, \ldots, \chi^j)$.
7. Update the Cholesky decomposition $\mathcal{D}_j$ of $\mathcal{COV}_j$.

solver. In the following, a BVP is applied to the square plate shown in Figure 3(a). We set

$A = 40\ m$ hence $\mathcal{B} = (0, 80)^2\ m^2$ that includes a predefined single notch $\mathcal{C}_1$ of length 8 m in the body center with $a = (36, 40)\ m$ and $b = (44, 40)\ m$, as depicted in Figure 3(a). A constant fluid flow of $\bar{f} = 0.03\ m^2/s$ is injected in $\mathcal{C}_1$. At the boundary $\partial_D\mathcal{B}$, all displacements are fixed in both directions and the fluid pressure is set to zero. Fluid injection $\bar{f}$ continues until failure for $T = 20$ seconds with time step $\Delta t = 0.1$ second during the simulation. The list of used computational and mechanical/geomechanical parameters, including their units is provided in Table 1.

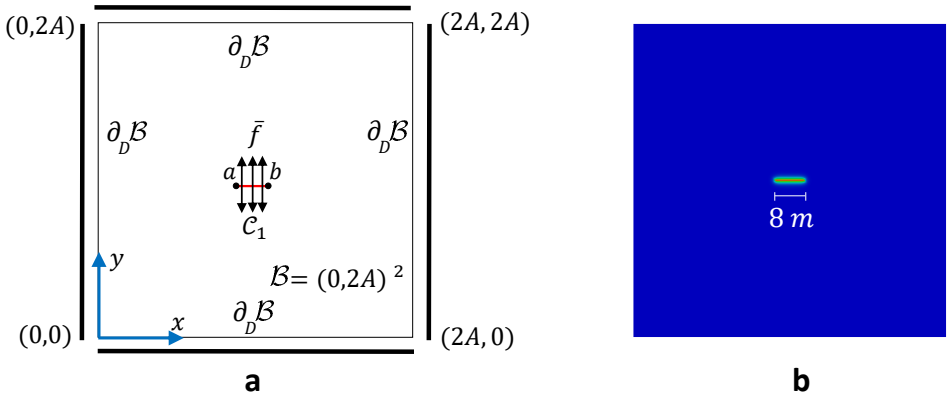

Figure 3: Hydraulically induced crack driven by fluid volume injection (a) Geometry and boundary conditions; and (b) described crack phase-field d as a Dirichlet boundary conditions at $t = 0\ s$.

We employ the DRAM algorithm to identify the parameters when both BI-SS and BI-GL techniques are used to estimate $\chi = (\lambda,\ \mu,\ G_c,\ M,\ B)$. The range of the parameters is given in Table 2. For our estimation, in each time-step, we define

$$\mathcal{P}^{\bullet} = \max_{\boldsymbol{x}\in\mathcal{B}} p(\boldsymbol{x}) \quad \text{with} \quad \bullet \in \{\text{SS,GL}\}, \tag{35}$$

denoting the maximum pressure during the fluid injection time. The maximum pressure will be used in the Bayesian estimation to produce the reference value and observations.

The evolution of the MCMC chains during different Bayesian inversion (BI) iterations are shown in Figure 4 and Figure 5 for BI-GL and BI-SS, respectively. The relative posterior destinies are depicted in Figure 6 and Figure 7. As shown, after several iterations all parameters converge to the true values pointing out the efficiency of the DRAM algorithm. The posterior densities have mainly normal distribution. Also, the true values (used to obtain the reference observation) are listed in Table 2 and shown with a dashed line. The medians of the posterior densities are mentioned in Table 2. Finally, we used the medians to solve the model equations using (SS) and (GL) methods. The maximum pressure ($\mathcal{P}^{\bullet}$) during different fluid injection times is shown in Figure 8. For both approaches, accurate estimations are obtained.

Table 1: Material parameters employed in the numerical experiments according to (Miehe and Mauthe, 2016; Xia et al., 2017). These values are related to material properties in our inferred observations.

No.	parameter	name	value	unit
1.	λ	Lamé's first parameter	11	GPa
2.	μ	shear modulus	6.65	GPa
3.	M	Biot's modulus	12.5	GPa
4.	B	Biot's coefficient	0.79	–
5.	K_D	Intrinsic permeability	2×10^{-14}	m^2
6.	η_F	Dynamic fluid viscosity	0.001	kg/(m.s)
7.	G_c	Griffith's energy release rate	0.0027	GPa
8.	η	Crack viscosity	10^{-14}	$\mathrm{N/m^2s}$
9.	κ	Stabilization parameter	10^{-8}	–
10.	ζ	Permeability transition exponent	50	–

Table 2: The computational features and the results of the BI-SS and BI-GL approaches.

Parameter	λ [GPa]	μ [GPa]	G_c [GPa]	M [GPa]	B
min	3	3	0.001	5	0.1
max	8	8	0.01	20	1
true value	4.43	6.65	0.0027	12.5	0.79
BI – SS	4.42	6.62	0.00267	12.87	0.8
BI – GL	4.45	6.70	0.0026	12.1	0.78

The numerical investigations indicate the accuracy of the BI-GL method. We estimate the reference value using the full model (the single-scale approach); however, the reduced model (global-local) obtained similar results. For the Bayesian inference, we used 200 iterations and compared the CPU (wall clock) time of both techniques. In Figure 9, we observed the computational time for different BI-iterations. Averagely, the BI-GL method has 31.62 times lower CPU time than BI-SS method. A comparison of the computational cost is provided in Table 3. It can be more pronounced in Bayesian estimation since many replications of the forward model are needed to reach a reasonable accuracy. A notable difference between the accumulation time $\sum_{i=1}^{N} T_i$ (with T_i represented as a CPU time for a froward model at the i^{th} iteration of Bayesian interface model) of both methods shows that the BI-GL technique is more suitable for parameter estimation.

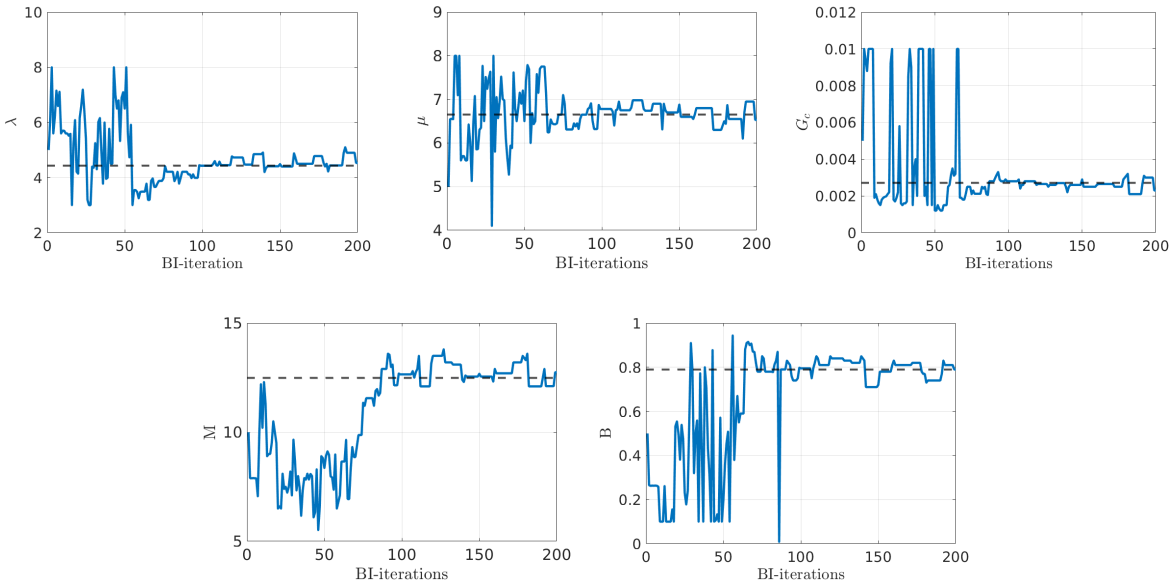

Figure 4: The convergence of the MCMC chains using the BI-GL approach. The true values are shown with a dashed black line.

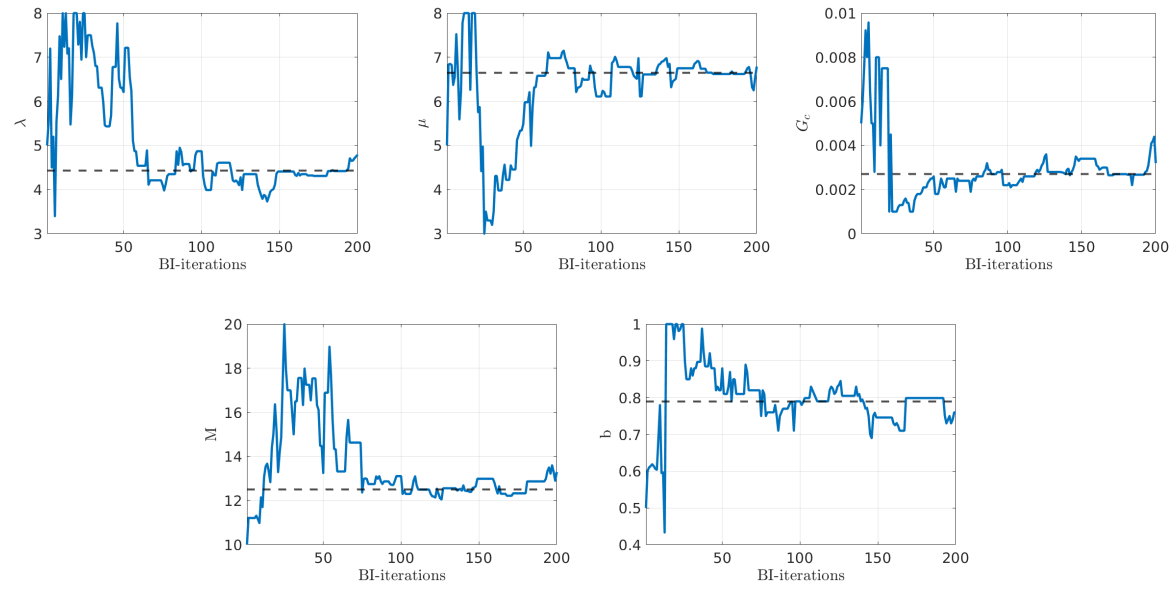

Figure 5: The convergence of the MCMC chains using the BI-SS approach. The true values are shown with a dashed black line.

For a better insight into the fracture process in BI-SS and BI-GL models, the evolution of the vertical displacment u_y, the fluid injection p, and the crack phase-field d are provided in Figure 10 and Figure 11, receptively, at different fluid injection time up to complete failure. Note that the solutions are based on the posterior density of the material parameters, which are given in Table 2. It can be grasped that, for both models, the crack initiates at the notch-tips due to fluid pressure increase. Thereafter, the crack propagates horizontally in two directions toward the boundaries. In conclusion, it is observed that the proposed BI-GL approach indeed yields results similar to the BI-SS solution (this includes the entire failure process simulation, as

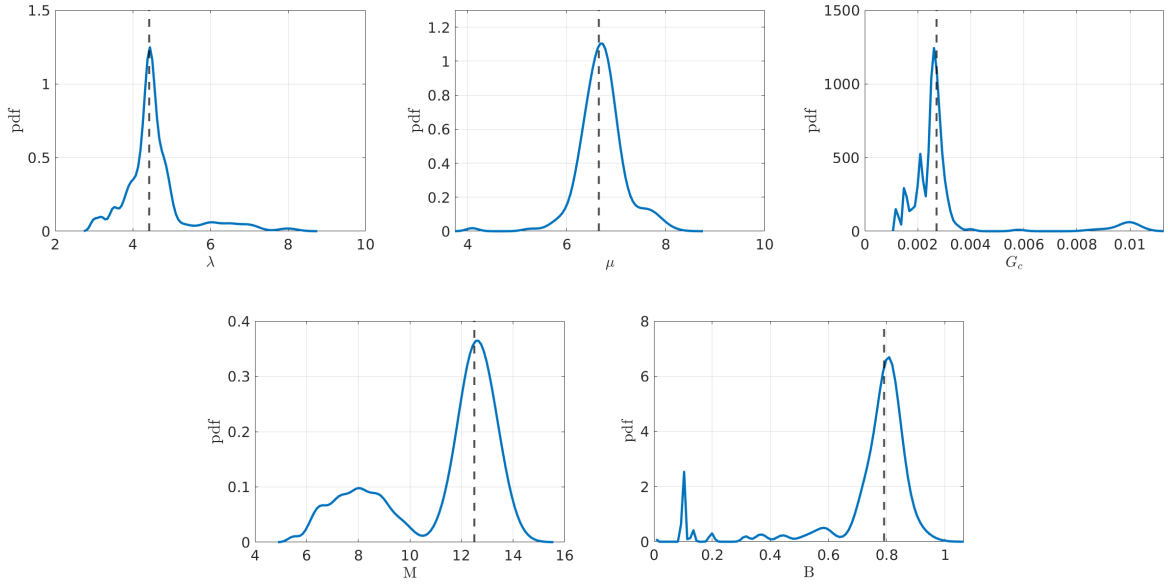

Figure 6: The pdf of posterior density of the material parameters using the BI-GL approach. The true values are shown with a dashed black line.

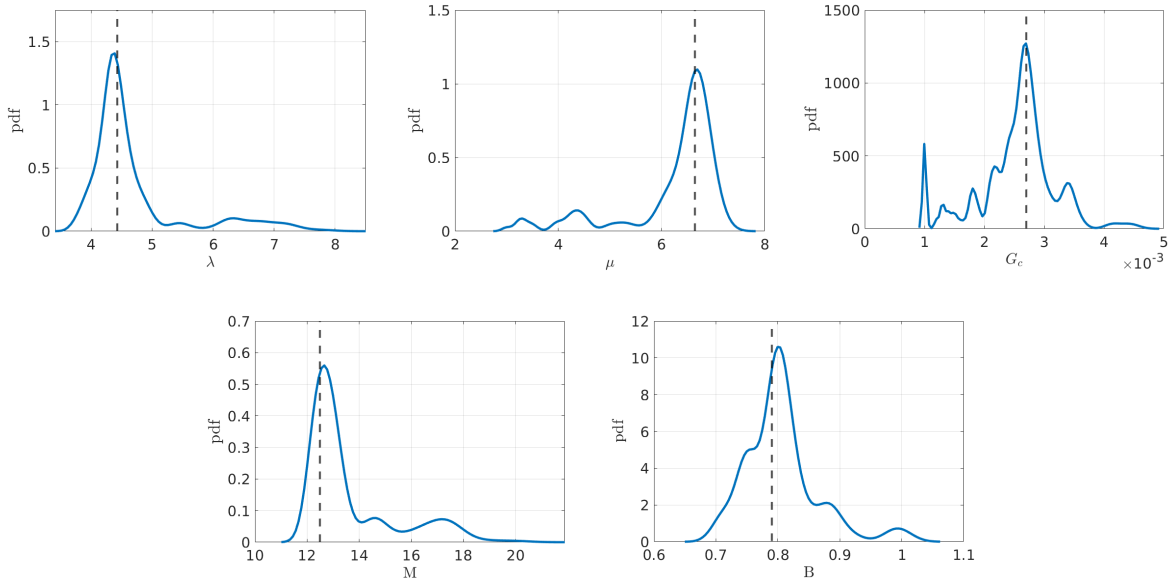

Figure 7: The pdf of posterior density of the material parameters using the BI-SS approach. The true values are shown with a dashed black line.

well as the maximum pressure vs. fluid injection time curves), yet they are obtained with much superior efficiency.

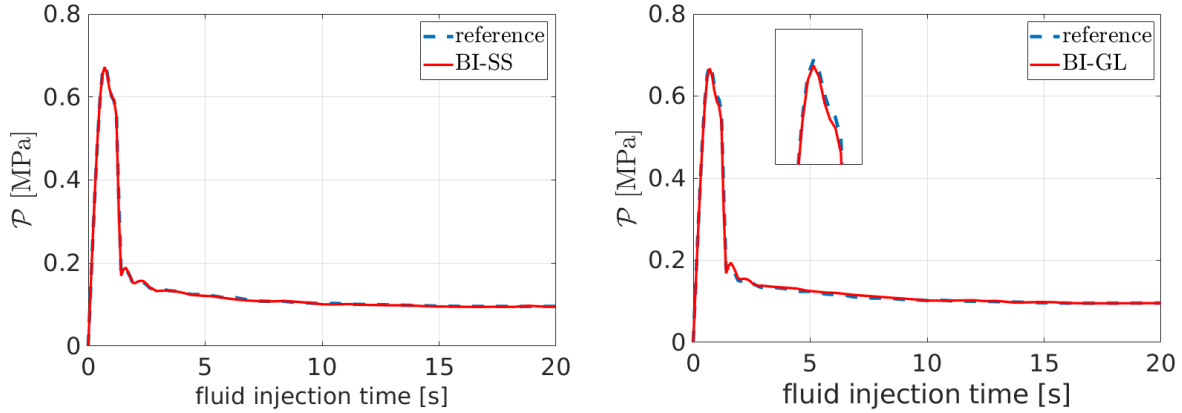

Figure 8: A comparison between the maximum pressure obtained by the true values (the reference observation) and the mean value of posterior density of BI-SS (left) and BI-GL (right).

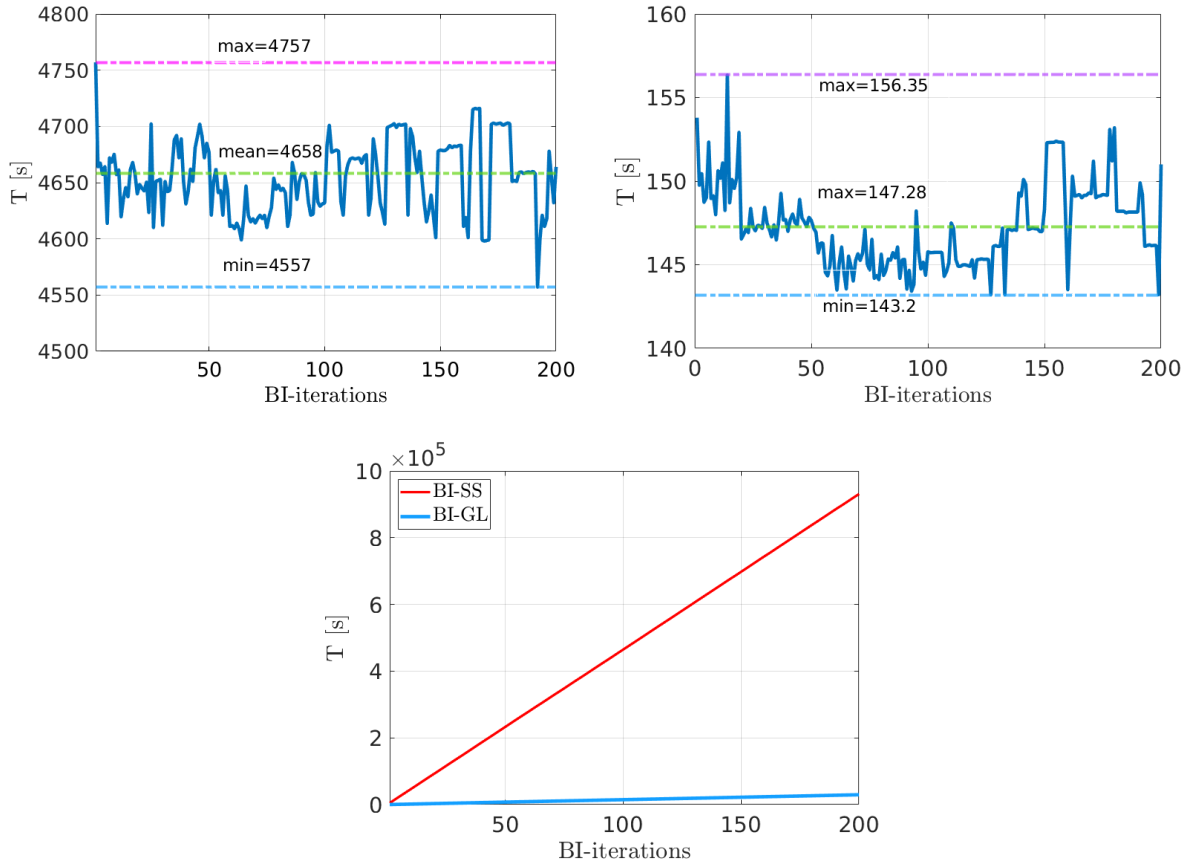

Figure 9: First line: The CPU time for different iterations using BI-SS (left) and BI-GL (right). We notice that the scalings of the ordinates are different. Second row: the accumulative time for both approaches.

Table 3: A comparison between the computational costs of BI-SS and BI-GL approaches. The unit is given in seconds.

Model	min T	max T	mean T	$\sum T$	ratio $T^\star$
BI – SS	4557	4757	4658	9.3×10^5	31.52
BI – GL	143.2	156.35	147.28	2.95×10^4	–

$$\star\ ratio := \frac{\sum T_{BI-SS}}{\sum T_{BI-GL}}\ .$$

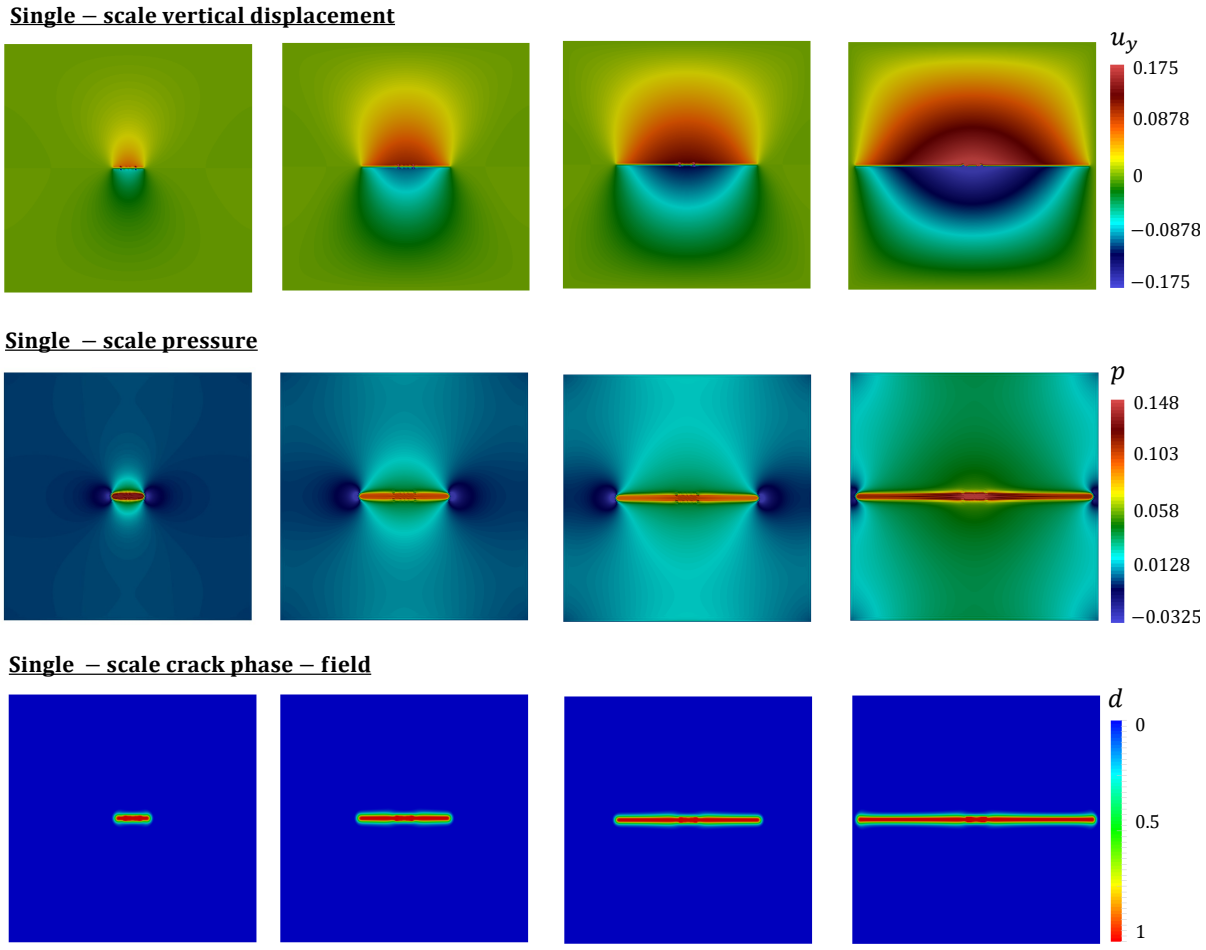

Figure 10: Single-scale results of the hydraulically induced crack driven by fluid volume injection. Evolution of the vertical displacement u_y (first row), fluid pressure p (second row) and crack phase-field d (third row) for different deformation stages up to final failure at $t = 1; 6.5; 13; 20$ seconds. These are based on the posterior density of the material parameters, which are given in Table 2.

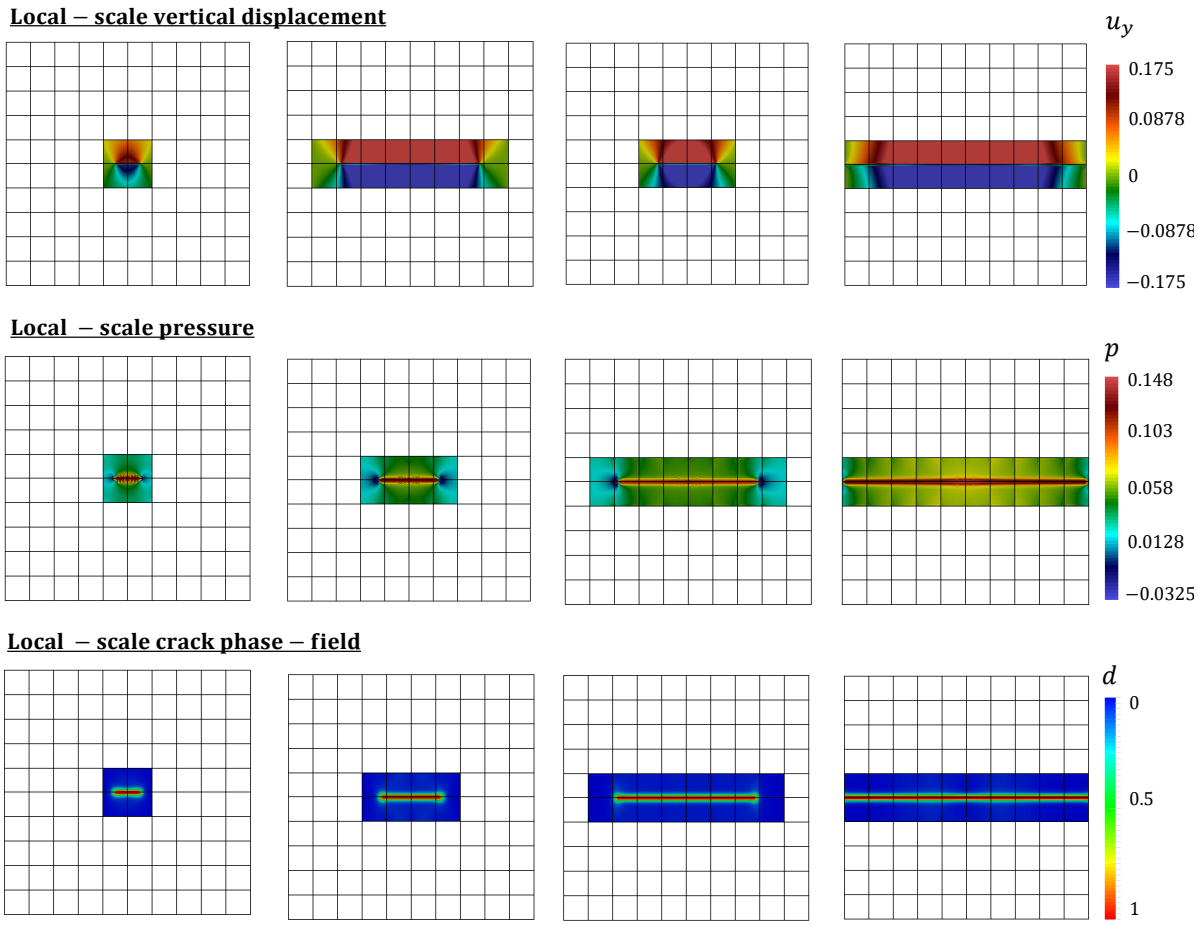

Figure 11: Local-scale results of the hydraulically induced crack driven by fluid volume injection. Evolution of the vertical displacement u_y (first row), fluid pressure p (second row), crack phase-field d (third row) for different fluid injection time steps at $t = 1; 6.5; 13; 20$ seconds up to final failure. These are based on the posterior density of the material parameters, which are given in Table 2.

6 Conclusions

In this work, we provided a proof of concept of using a phase-field global-local formulation as the forward model with Bayesian inversion. Therein, a phase-field model coupled with Darcy-type flow can be used to model the fracture and the pressure. To obtain a reasonable estimation of the crack profile several degrees of freedom are needed which increase the problem complexity. The mechanical and geomechanical parameters have a significant effect on the simulations. However, due to the spatial fluctuation, a reliable estimation of the material parameters can not be experimentally estimated. Bayesian inversion is an effective tool to provide information about the parameters. Here, the main challenge is that the forward model is computationally expensive, i.e., one replication takes more than one hour.

As resort, we proposed the idea of using a global-local setting enhanced with a predictor-corrector mesh refinement approach to model the hydraulic fracture and identify the parameters. Instead of solving the problem in the whole domain (single-scale formulation), a significant computational time reduction has been achieved by solving the problem in fewer degrees of

freedom (global-local approach). Mainly, because the local domain is dynamically adjusted to the current fracture state. After the design of the algorithmic concept, we investigated in great detail the accuracy and efficiency in some numerical simulations with application in hydraulic fracture propagation in porous media. Our observations indicated that the Bayesian inversion using global-local forward model BI-GL is 32 times faster than the BI-SS model, although the accuracy is similar.

As future work, we are mainly interested in exploring more examples in solid mechanics, multiple interacting fractures, and fractures in thermoporoelasticity. Also, the combination of adaptive schemes and parallel computing will be addressed.

Acknowledgment

N. Noii were founded by the Priority Program DFG SPP 2020 that is *Cyclical Damage Processes in high-Performance Concrete* within its second funding phase. T. Wick has been supported by the German Research Foundation, Priority Program 1962 (DFG SPP 1962) with in the subproject *Optimizing Fracture Propagation using a Phase-Field Approach* with the project number 314067056

References

Abbaszadeh, M., Dehghan, M., Khodadadian, A., Noii, N., Heitzinger, C., and Wick, T., A reduced-order variational multiscale interpolating element free galerkin technique based on proper orthogonal decomposition for solving navier–stokes equations coupled with a heat transfer equation: Nonstationary incompressible boussinesq equations, *Journal of Computational Physics*, vol. **426**, p. 109875, 2021.

Aldakheel, F., Noii, N., Wick, T., Allix, O., and Wriggers, P., Multilevel global-local techniques for adaptive ductile phase-field fracture, *Computer Methods in Applied Mechanics and Engineering*, vol. **387**, p. 114175, 2021a.

Aldakheel, F., Noii, N., Wick, T., and Wriggers, P., A global-local approach for hydraulic phase-field fracture in poroelastic media, *Computers & Mathematics with Applications*, vol. **91**, pp. 99–121, 2021b, robust and Reliable Finite Element Methods in Poromechanics.

Almani, T., Kumar, K., Dogru, A., Singh, G., and Wheeler, M., Convergence analysis of multirate fixed-stress split iterative schemes for coupling flow with geomechanics, *Computer Methods in Applied Mechanics and Engineering*, vol. **311**, pp. 180–207, 2016.
URL `https://www.sciencedirect.com/science/article/pii/S0045782516308180`

Almani, T., Kumar, K., and Manea, A., On the convergence of flow and mechanics iterative coupling schemes in fractured heterogeneous poro-elastic media, *Numerical Mathematics and Advanced Applications ENUMATH 2019*, Vermolen, F.J. and Vuik, C. (Eds.), Springer International Publishing, Cham, pp. 53–62, 2021.

Altmann, R., Maier, R., and Unger, B., Semi-explicit discretization schemes for weakly coupled elliptic-parabolic problems, *Math. Comp.*, vol. **90**, no. 329, pp. 1089–1118, 2021.

Both, J., Borregales, M., Nordbotten, J., Kumar, K., and Radu, F., Robust fixed stress splitting for biot's equations in heterogeneous media, *Applied Mathematics Letters*, vol. **68**, pp. 101 – 108, 2017.
URL `http://www.sciencedirect.com/science/article/pii/S0893965917300034`

Bourdin, B., Numerical implementation of the variational formulation for quasi-static brittle fracture, *Interfaces and free boundaries*, vol. **9**, pp. 411–430, 2007.

Bourdin, B., Francfort, G., and Marigo, J.J., The variational approach to fracture, *J. Elasticity*, vol. **91**, no. 1-3, pp. 1–148, 2008.

Bourdin, B. and Francfort, G.A., Past and present of variational fracture, *SIAM News*, vol. **52**, no. 9, 2019.

Brun, M.K., Wick, T., Berre, I., Nordbotten, J.M., and Radu, F.A., An iterative staggered scheme for phase field brittle fracture propagation with stabilizing parameters, *Computer Methods in Applied Mechanics and Engineering*, vol. **361**, p. 112752, 2020.

Castelletto, N., White, J.A., and Tchelepi, H.A., Accuracy and convergence properties of the fixed-stress iterative solution of two-way coupled poromechanics, *International Journal for Numerical and Analytical Methods in Geomechanics*, vol. **39**, no. 14, pp. 1593–1618, 2015.
URL `http://dx.doi.org/10.1002/nag.2400`

Chen, B., Barboza, B.R., Sun, Y., Bai, J., Thomas, H.R., Dutko, M., Cottrell, M., and Li, C., A review of hydraulic fracturing simulation, *Archives of Computational Methods in Engineering*, pp. 1–58, 2021.

Chukwudozie, C., Bourdin, B., and Yoshioka, K., A variational phase-field model for hydraulic fracturing in porous media, *Computer Methods in Applied Mechanics and Engineering*, vol. **347**, pp. 957 – 982, 2019.
URL `http://www.sciencedirect.com/science/article/pii/S0045782518306443`

Dana, S., Ganis, B., and Wheeler, M.F., A multiscale fixed stress split iterative scheme for coupled flow and poromechanics in deep subsurface reservoirs, *Journal of Computational Physics*, vol. **352**, pp. 1–22, 2018.

Dana, S., Jammoul, M., and Wheeler, M.F., Performance studies of the fixed stress split algorithm for immiscible two-phase flow coupled with linear poromechanics, *Computational Geosciences*, pp. 1–15, 2021.

Dana, S. and Wheeler, M.F., Convergence analysis of fixed stress split iterative scheme for anisotropic poroelasticity with tensor biot parameter, *Computational Geosciences*, vol. **22**, no. 5, pp. 1219–1230, 2018a.

Dana, S. and Wheeler, M.F., Convergence analysis of two-grid fixed stress split iterative scheme for coupled flow and deformation in heterogeneous poroelastic media, *Computer Methods in Applied Mechanics and Engineering*, vol. **341**, pp. 788–806, 2018b.

Dean, R., Gai, X., Stone, C., and Minkoff, S., A comparison of techniques for coupling porous flow and geomechanics, *SPE-79709-MS*, pp. 132–140, 2006.

Evensen, G., The ensemble Kalman filter for combined state and parameter estimation, *IEEE Control Systems Magazine*, vol. **29**, no. 3, pp. 83–104, 2009.

Francfort, G., Variational fracture: twenty years after, *International Journal of Fracture*, pp. 1–11, 2021.

Geelen, R., Plews, J., Tupek, M., and Dolbow, J., An extended/generalized phase-field finite element method for crack growth with global-local enrichment, *International Journal for Numerical Methods in Engineering*, vol. **121**, no. 11, pp. 2534–2557, 2020.
URL `https://onlinelibrary.wiley.com/doi/abs/10.1002/nme.6318`

Gerasimov, T. and Lorenzis, L.D., A line search assisted monolithic approach for phase-field computing of brittle fracture, *Computer Methods in Applied Mechanics and Engineering*, vol. **312**, pp. 276 – 303, 2016.

Gerasimov, T., Noii, N., Allix, O., and De Lorenzis, L., A non-intrusive global/local approach applied to phase-field modeling of brittle fracture, *Advanced Modeling and Simulation in Engineering Sciences*, vol. **5**, no. 1, p. 14, 2018.

Gerasimov, T., Römer, U., Vondřejc, J., Matthies, H.G., and De Lorenzis, L., Stochastic phase-field modeling of brittle fracture: computing multiple crack patterns and their probabilities, *Computer Methods in Applied Mechanics and Engineering*, vol. **372**, p. 113353, 2020.

Girault, V., Kumar, K., and Wheeler, M., Convergence of iterative coupling of geomechanics with flow in a fractured poroelastic medium, *Computational Geosciences*, vol. **20**, no. 5, pp. 997–1011, 2016.

Green, P. and Worden, K., Bayesian and Markov chain Monte Carlo methods for identifying nonlinear systems in the presence of uncertainty, *Philosophical Transactions of the Royal Society A: Mathematical, Physical and Engineering Sciences*, vol. **373**, no. 2051, p. 20140405, 2015.

Green, P.J. and Mira, A., Delayed rejection in reversible jump Metropolis–Hastings, *Biometrika*, vol. **88**, no. 4, pp. 1035–1053, 2001.

Haario, H., Laine, M., Mira, A., and Saksman, E., DRAM: efficient adaptive MCMC, *Statistics and computing*, vol. **16**, no. 4, pp. 339–354, 2006.

Haario, H., Saksman, E., and Tamminen, J., Adaptive proposal distribution for random walk metropolis algorithm, *Computational Statistics*, vol. **14**, no. 3, pp. 375–395, 1999.

Heider, Y., A review on phase-field modeling of hydraulic fracturing, *Engineering Fracture Mechanics*, vol. **253**, p. 107881, 2021.
URL `https://www.sciencedirect.com/science/article/pii/S0013794421003143`

Heider, Y. and Markert, B., A phase-field modeling approach of hydraulic fracture in saturated porous media, *Mechanics Research Communications*, vol. **80**, pp. 38 – 46, 2017, multi-Physics of Solids at Fracture.
URL `http://www.sciencedirect.com/science/article/pii/S0093641316300714`

Heider, Y., Reiche, S., Siebert, P., and Markert, B., Modeling of hydraulic fracturing using a porous-media phase-field approach with reference to experimental data, *Engineering Fracture Mechanics*, vol. **202**, pp. 116 – 134, 2018.
URL `http://www.sciencedirect.com/science/article/pii/S0013794418306192`

Hong, Q. and Kraus, J., Parameter-robust stability of classical three-field formulation of biot's consolidation model, *ETNA - Electronic Transactions on Numerical Analysis*, vol. **48**, pp. 202–226, 2018.
URL `http://dx.doi.org/10.1553/etna_vol48s202`

Hong, Q., Kraus, J., Lymbery, M., and Wheeler, M.F., Parameter-robust convergence analysis of fixed-stress split iterative method for multiple-permeability poroelasticity systems, *Multiscale Modeling & Simulation*, vol. **18**, no. 2, pp. 916–941, 2020.

Jammoul, M., Wheeler, M.F., and Wick, T., A phase-field multirate scheme with stabilized iterative coupling for pressure driven fracture propagation in porous media, *Computers & Mathematics with Applications*, vol. **91**, pp. 176–191, 2021, robust and Reliable Finite Element Methods in Poromechanics.
URL `https://www.sciencedirect.com/science/article/pii/S089812212030434X`

Jodlbauer, D., Parallel Multigrid Solvers for Nonlinear Coupled Field Problems, PhD thesis, Johannes Kepler University Linz, 2021.

Jodlbauer, D., Langer, U., and Wick, T., Matrix-free multigrid solvers for phase-field fracture problems, *Computer Methods in Applied Mechanics and Engineering*, vol. **372**, p. 113431, 2020a.
URL `http://www.sciencedirect.com/science/article/pii/S0045782520306162`

Jodlbauer, D., Langer, U., and Wick, T., Parallel matrix-free higher-order finite element solvers for phase-field fracture problems, *Mathematical and Computational Applications*, vol. **25**, no. 3, p. 40, 2020b.

Khimin, D., Steinbach, M.C., and Wick, T., 2021. Optimal control for phase-field fracture: Algorithmic concepts and computations, preprint SPP1962-160.

Khodadadian, A., Noii, N., Parvizi, M., Abbaszadeh, M., Wick, T., and Heitzinger, C., A bayesian estimation method for variational phase-field fracture problems, *Computational Mechanics*, vol. **66**, pp. 827–849, 2020.

Kim, J., Tchelepi, H., and Juanes, R., Stability and convergence of sequentiel methods for coupled flow and geomechanics: fixed-stress and fixed-strain splits, *Comp. Methods Appl. Mech. Engrg.*, vol. **200**, no. 13-16, pp. 1591–1606, 2011.

Kopanicakova, A. and Krause, R., A recursive multilevel trust region method with application to fully monolithic phase-field models of brittle fracture, *Computer Methods in Applied Mechanics and Engineering*, vol. **360**, p. 112720, 2020.
URL http://www.sciencedirect.com/science/article/pii/S0045782519306085

Kristensen, P.K. and MartÃnez-Paneda, E., Phase field fracture modelling using quasi-newton methods and a new adaptive step scheme, *Theoretical and Applied Fracture Mechanics*, vol. **107**, p. 102446, 2020.
URL https://www.sciencedirect.com/science/article/pii/S0167844219305580

Lampron, O., Therriault, D., and LÃ©vesque, M., An efficient and robust monolithic approach to phase-field quasi-static brittle fracture using a modified newton method, *Computer Methods in Applied Mechanics and Engineering*, vol. **386**, p. 114091, 2021.
URL http://dx.doi.org/10.1016/j.cma.2021.114091

Lecampion, B., Bunger, A., and Zhang, X., Numerical methods for hydraulic fracture propagation: A review of recent trends, *Journal of Natural Gas Science and Engineering*, vol. **49**, pp. 66–83, 2018.
URL https://www.sciencedirect.com/science/article/pii/S1875510017304006

Lee, S., Wheeler, M.F., and Wick, T., Pressure and fluid-driven fracture propagation in porous media using an adaptive finite element phase field model, *Computer Methods in Applied Mechanics and Engineering*, vol. **305**, pp. 111 – 132, 2016.

Lee, S., Wheeler, M.F., and Wick, T., Iterative coupling of flow, geomechanics and adaptive phase-field fracture including level-set crack width approaches, *Journal of Computational and Applied Mathematics*, vol. **314**, pp. 40 – 60, 2017.
URL http://www.sciencedirect.com/science/article/pii/S0377042716305118

Lu, X. and Wheeler, M.F., Three-way coupling of multiphase flow and poromechanics in porous media, *Journal of Computational Physics*, vol. **401**, p. 109053, 2020.
URL https://www.sciencedirect.com/science/article/pii/S0021999119307582

Mauthe, S. and Miehe, C., Hydraulic fracture in poro-hydro-elastic media, *Mechanics Research Communications*, vol. **80**, pp. 69–83, 2017.

Mesgarnejad, A., Bourdin, B., and Khonsari, M., Validation simulations for the variational approach to fracture, *Computer Methods in Applied Mechanics and Engineering*, vol. **290**, pp. 420 – 437, 2015.

Miehe, C., Hofacker, M., and Welschinger, F., A phase field model for rate-independent crack propagation: Robust algorithmic implementation based on operator splits, *Comput. Meth. Appl. Mech. Engrg.*, vol. **199**, pp. 2765–2778, 2010.

Miehe, C. and Mauthe, S., Phase field modeling of fracture in multi-physics problems. part iii. crack driving forces in hydro-poro-elasticity and hydraulic fracturing of fluid-saturated porous media, *Computer Methods in Applied Mechanics and Engineering*, vol. **304**, pp. 619–655, 2016.

Miehe, C., Schaenzel, L.M., and Ulmer, H., Phase field modeling of fracture in multi-physics problems. part i. balance of crack surface and failure criteria for brittle crack propagation in thermo-elastic solids, *Computer Methods in Applied Mechanics and Engineering*, vol. **294**, pp. 449–485, 2015.

Mikelić, A., Wheeler, M., and Wick, T., 2013. A phase-field approach to the fluid filled fracture surrounded by a poroelastic medium, iCES Report 13-15.

Mikelić, A. and Wheeler, M.F., Convergence of iterative coupling for coupled flow and geomechanics, *Comput Geosci*, vol. **17**, no. 3, pp. 455–462, 2012.

Mikelić, A., Wheeler, M.F., and Wick, T., A phase-field method for propagating fluid-filled fractures coupled to a surrounding porous medium, *SIAM Multiscale Model. Simul.*, vol. **13**, no. 1, pp. 367–398, 2015.

Mikelić, A., Wheeler, M.F., and Wick, T., Phase-field modeling of a fluid-driven fracture in a poroelastic medium, *Computational Geosciences*, vol. **19**, no. 6, pp. 1171–1195, 2015.
URL http://dx.doi.org/10.1007/s10596-015-9532-5

Mikelić, A., Wheeler, M.F., and Wick, T., Phase-field modeling through iterative splitting of hydraulic fractures in a poroelastic medium, *GEM - International Journal on Geomathematics*, vol. **10**, no. 1, 2019.

Mohammadi, M. and Wollner, W., Phase field modelling of fracture, *Optimization and Engineering*, 2020.

Neitzel, I., Wick, T., and Wollner, W., An optimal control problem governed by a regularized phase-field fracture propagation model, *SIAM Journal on Control and Optimization*, vol. **55**, no. 4, pp. 2271–2288, 2017.

Neitzel, I., Wick, T., and Wollner, W., An optimal control problem governed by a regularized phase-field fracture propagation model. part ii: The regularization limit, *SIAM Journal on Control and Optimization*, vol. **57**, no. 3, pp. 1672–1690, 2019.

Noii, N. and Aghayan, I., Characterization of elastic-plastic coated material properties by indentation techniques using optimisation algorithms and finite element analysis, *International Journal of Mechanical Sciences*, vol. **152**, pp. 465–480, 2019.

Noii, N., Aldakheel, F., Wick, T., and Wriggers, P., An adaptive global-local approach for phase-field modeling of anisotropic brittle fracture, *Computer Methods in Applied Mechanics and Engineering*, vol. **361**, p. 112744, 2020.
URL `http://www.sciencedirect.com/science/article/pii/S0045782519306346`

Noii, N., Fan, M., Wick, T., and Jin, Y., A quasi-monolithic phase-field description for orthotropic anisotropic fracture with adaptive mesh refinement and primal-dual active set method, *Engineering Fracture Mechanics*, p. 108060, 2021a.

Noii, N., Khodadadian, A., Ulloa, J., Aldakheel, F., Wick, T., Francois, S., and Wriggers, P., Bayesian inversion for unified ductile phase-field fracture, *Computational Mechanics*, 2021b.

Noii, N., Khodadadian, A., and Wick, T., Bayesian inversion for anisotropic hydraulic phase-field fracture, *Computer Methods in Applied Mechanics and Engineering*, vol. **386**, p. 114118, 2021c.

Noii, N. and Wick, T., A phase-field description for pressurized and non-isothermal propagating fractures, *Computer Methods in Applied Mechanics and Engineering*, vol. **351**, pp. 860 – 890, 2019.
URL `http://www.sciencedirect.com/science/article/pii/S0045782519301975`

Santillan, D., Juanes, R., and Cueto-Felgueroso, L., Phase field model of fluid-driven fracture in elastic media: Immersed-fracture formulation and validation with analytical solutions, *Journal of Geophysical Research: Solid Earth*, vol. **122**, no. 4, pp. 2565–2589, 2017, 2016JB013572.
URL `http://dx.doi.org/10.1002/2016JB013572`

Settari, A. and Mourits, F., A coupled reservoir and geomechanical simulation system, *SPE Journal*, vol. **3**, no. 3, pp. 219–226, 1998.

Settari, A. and Walters, D.A., Advances in coupled geomechanical and reservoir modeling with applications to reservoir compaction, *SPE Journal*, vol. **6**, no. 3, pp. 334–342, 2001.

Smith, R.C., *Uncertainty quantification: theory, implementation, and applications*, Vol. 12, SIAM, 2013.

Wambacq, J., Ulloa, J., Lombaert, G., and Francois, S., Interior-point methods for the phase-field approach to brittle and ductile fracture, *Computer Methods in Applied Mechanics and Engineering*, vol. **375**, p. 113612, 2021.

Wheeler, M.F., Wick, T., and Lee, S., IPACS: Integrated Phase-Field Advanced Crack Propagation Simulator. An adaptive, parallel, physics-based-discretization phase-field framework for fracture propagation in porous media, *Computer Methods in Applied Mechanics and Engineering*, vol. **367**, p. 113124, 2020.

Wick, T., An error-oriented Newton/inexact augmented Lagrangian approach for fully monolithic phase-field fracture propagation, *SIAM Journal on Scientific Computing*, vol. **39**, no. 4, pp. B589–B617, 2017a.

Wick, T., Modified Newton methods for solving fully monolithic phase-field quasi-static brittle fracture propagation, *Computer Methods in Applied Mechanics and Engineering*, vol. **325**, pp. 577 – 611, 2017b.

Wick, T., *Multiphysics Phase-Field Fracture: Modeling, Adaptive Discretizations, and Solvers*, De Gruyter, Berlin, Boston, 2020.

Wilson, Z.A. and Landis, C.M., Phase-field modeling of hydraulic fracture, *Journal of the Mechanics and Physics of Solids*, vol. **96**, pp. 264 – 290, 2016.

Wu, J.Y., Nguyen, V.P., Thanh Nguyen, C., Sutula, D., Bordas, S., and Sinaie, S., Phase field modelling of fracture, *Advances in Applied Mechanics*, vol. **53**, 2019.

Wu, T., Rosic, B., de Lorenzis, L., and Matthies, H., Parameter identification for phase-field modeling of fracture: a bayesian approach with sampling-free update, *Computational Mechanics*, vol. **67**, pp. 435–453, 2021.

Xia, L., Yvonnet, J., and Ghabezloo, S., Phase field modeling of hydraulic fracturing with interfacial damage in highly heterogeneous fluid-saturated porous media, *Engineering Fracture Mechanics*, vol. **186**, pp. 158–180, 2017.

Yoshioka, K. and Bourdin, B., A variational hydraulic fracturing model coupled to a reservoir simulator, *International Journal of Rock Mechanics and Mining Sciences*, vol. **88**, pp. 137 – 150, 2016.
URL `http://www.sciencedirect.com/science/article/pii/S1365160916301484`